Chemical Science

ROYAL SOCIETY OF CHEMISTRY

EDGE ARTICLE

View Article Online
View Journal | View Issue

Cite this: *Chem. Sci.*, 2024, **15**, 9298

All publication charges for this article have been paid for by the Royal Society of Chemistry

Received 19th February 2024
Accepted 10th May 2024

DOI: 10.1039/d4sc01180e

rsc.li/chemical-science

Sulphur-atom positional engineering in perylenimide: structure–property relationships and H-aggregation directed type-I photodynamic therapy†

Mst Nasima Khatun, [a] Satyendu Nandy, [b] Hirakjyoti Roy, [c] Siddhartha Sankar Ghosh, *[bc] Sachin Kumar *[b] and Parameswar Krishnan Iyer *[ac]

An innovative design strategy of placing sulfur (S)-atoms within the pendant functional groups and at carbonyl positions in conventional perylenimide (**PNI-O**) has been demonstrated to investigate the condensed state structure–property relationship and potential photodynamic therapy (PDT) application. Incorporation of simply S-atoms at the *peri*-functionalized perylenimide (**RPNI-O**) leads to an aggregation-induced enhanced emission luminogen (AIEEgen), 2-hexyl-8-(thianthren-1-yl)-1*H*-benzo[5,10]anthra[2,1,9-def]isoquinoline-1,3(2*H*)-dione (**API**), which achieves a remarkable photoluminescence quantum yield (Φ_{PL}) of 0.85 in aqueous environments and established novel AIE mechanisms. Additionally, substitution of the S-atom at the carbonyl position in **RPNI-O** leads to thioperylenimides (**RPNI-S**): 2-hexyl-8-phenyl-1*H*-benzo[5,10]anthra[2,1,9-def]isoquinoline-1,3(2*H*)-dithione (**PPIS**), 8-([2,2′-bithiophen]-5-yl)-2-hexyl-1*H*-benzo[5,10]anthra[2,1,9-def]isoquinoline-1,3(2*H*)-dithione (**THPIS**), and 2-hexyl-8-(thianthren-1-yl)-1*H*-benzo[5,10]anthra[2,1,9-def]isoquinoline-1,3(2*H*)-dithion (**APIS**), with distinct photophysical properties (enlarged spin–orbit coupling (SOC) and $\Phi_{PL} \approx 0.00$), and developed diverse potent photosensitizers (PSs). The present work provides a novel SOC enhancement mechanism *via* pronounced H-aggregation. Surprisingly, the lowest singlet oxygen quantum yield (Φ_{Δ}) and theoretical calculation suggest the specific type-I PDT for **RPNI-S**. Interestingly, **RPNI-S** efficiently produces superoxide ($O_2^{\bullet-}$) due to its remarkably lower Gibbs free energy (ΔG) values (**THPIS**: −40.83 kcal mol^{-1}). The non-toxic and heavy-atom free very specific thio-based **PPIS** and **THPIS** PSs showed selective and efficient PDT under normoxia, as a rare example.

Introduction

In recent years, PDT, a photochemical reaction-based treatment that utilizes light with appropriate PSs, has attracted significant attention due to its distinct advantages over most conventional therapies in cancer treatments.[1,2] Yet, classical PSs have low excited state triplet formation, and the introduction of heavy-atoms to enlarge SOC and subsequently enhance intersystem crossing (ISC) into their structures often raises significant concerns about cost and high dark toxicity.[3,4] In PDT, two distinct mechanisms, type-I and type-II, govern the reactions of PSs with ground-state oxygen ($^3O_2$). Type-I PDT involves the intermolecular electron transfer (IET) process, which transfers an electron from the triplet excitons of the PS to $^3O_2$, leading to the formation of $O_2^{\bullet-}$. This process can occur independently of any reducing intermediary, generating hydrogen peroxide (H_2O_2) and hydroxyl radicals (HO$^{\bullet}$) through superoxide disproportionation and the Franck–Condon transition.[5] Crucially, this reaction requires an allowed electron transfer, indicated by a negative Gibbs free energy change ($\Delta G < 0$).[6] Conversely, type-II PDT relies on the energy transfer from PS triplet excitons to $^3O_2$, forming $^1O_2$. Comparatively, the type-I process in PDT mechanisms is more advantageous due to its lower dependence on oxygen content, and it remains relatively rare to date.[7,8] The S-substituted nucleobase anticancer drugs have received increasing interest in the past few decades due to their potential

[a]*Department of Chemistry, Indian Institute of Technology Guwahati, Guwahati 781039, Assam, India. E-mail: pki@iitg.ac.in; Fax: +91-3612582349*

[b]*Department of Biosciences and Bioengineering, Indian Institute of Technology Guwahati, Guwahati 781039, Assam, India*

[c]*Centre for Nanotechnology, Indian Institute of Technology Guwahati, Guwahati 781039, Assam, India*

† Electronic supplementary information (ESI) available: Materials, instrumentation, methods, synthetic procedures, and characterization data (including multinuclear NMR and MALDI-TOF). Further experimental and computational data, including Schemes S1–S4, Fig. S1–S24, supporting Fig. S25–S48 and Tables S1–S25. CCDC 2325822, 2325824 and 2325826. For ESI and crystallographic data in CIF or other electronic format see DOI: https://doi.org/10.1039/d4sc01180e

chemotherapeutic applications. They are still being explored for their potential new therapeutic abilities.[9–11] Additionally, the excellent excited triplet formation triggered by the thiocarbonyl group of thiobase PSs could result in more prospective PSs with promising PDT applications. However, numerous drawbacks of thiobase drugs, including long irradiation times, the need for higher concentrations, *etc.*, have limited their obvious practical applications.[12,13] Yet, numerous S-substituted derivatives in the carbonyl group have been comprehensively designed as heavy-atom-free materials.[14,15] The development of such an S-substituted carbonyl group in tumor treatment has not been extensively studied. This motivated us to reflect upon the thionation approach for future exploration of PSs with clinical acceptance. While heavy-atom-free thio-based naphthalimide (**NI**) PSs were designed for hypoxic environments, they lack specificity, selectivity, and HO$^{\bullet}$ generation ability. The study did not thoroughly explore type-I mechanisms and varied PS production. It was limited to one cell line, raising questions about broader applicability. Additional targeting agents were needed for prior heavy-atom-free PSs in biological environments. The absence of an S-atom at a functional position in their design is noteworthy, as it may significantly impact PDT-mediated cancer treatment and other unique properties, rather than solely relying on PDT applications (Table S1†).[14]

Considering these insights, the **PNI-O** core has been chosen as the potent core due to its exceptional Φ_{PL}, chemical stability, and thermal resilience, as well as its promising potential applications in various fields, including sensors,[16] therapeutics,[17] optoelectronics,[18] and bioimaging.[19] Further, an innovative design strategy involving the incorporation of S-atoms into both pendant functional groups and carbonyl positions within a planar **PNI-O** core, distinct from the previous thio-based approach, has been demonstrated here. The aim is to explore the structure–property relationship in the condensed state, especially in the context of potential PDT applications for cancer treatment. This investigation aligns with a well-established and ongoing effort to understand condensed state structure–property relationships, driven by their significance across various fields. Incorporating S-atoms at both the functional and carbonyl positions results in distinct properties within **PNI-O**. The introduction of simple S-atoms at functional positions triggers a unique transformation from aggregation-caused quenching (ACQ)-to-AIEE behavior within the extremely planar **PNI-O** core, which results in Φ_{PL} of 0.85 (with unique microrose supramolecular-assembly) and a significant Stokes shift of 146 nm, which are rarely observed. This modification also establishes a novel AIE mechanism. While S-atoms at the carbonyl position led to a complete drop in the fluorescence intensity ($\Phi_{PL} \approx 0.00$) and enlarged SOC, it promoted type-I PDT reactions with efficient production of $O_2^{\bullet-}$. This strategy demonstrates broad PDT applicability, targeting cancer cells (HeLa and MCF7) and normal cells without additional targeting agents, emphasizing its newer therapeutic ability and cost-effectiveness. Notably, the biocompatible heavy-atom-free thio-based PSs exhibit selective and efficient PDT efficacy, marking the first reported instance. This work provides SOC enhancement mechanisms through prominent H-aggregation (Table S2†). While previous research showed improved SOC and ISC, this research unveils the critical role of pronounced H-aggregation in this enhancement, opening up new possibilities for future PS design.[14,15] This approach allows for precise control over the generation of distinct variations of type-I and type-II ROS, expanding the potential applications of these PSs.

Hence, this research introduces a novel concept of condensed state emitters and highly specific and selective heavy-atom-free thio-based PSs, exhibiting a simple and precise platform to manipulate condensed state emissions, supramolecular assembly, and unique PS development, marking significant progress in the field.

Results and discussion

Design, synthesis, and characterization of RPNI-O and RPNI-S derivatives

The primary objective of this research was to explore the unique condensed state photophysical behavior and the photosensitizing capabilities of newly designed heavy-atom-free **RPNI-O** and **RPNI-S**. To achieve this, **RPNI-O** (**PPI**, **THPI**, and **API**) and **RPNI-S** (**PPIS**, **THPIS**, and **APIS**) have been strategically developed by introducing S-atom positional engineering at the pendant functional group and carbonyl position in the **PNI-O** core (Schemes 1 and S1–S4†). For the synthesis, very economical perylene-3,4,9,10-tetracarboxylic acid anhydride (**PDA**) was selected as a versatile precursor material, which underwent a condensation reaction with hexylamine in good yields (Scheme S1†). Subsequently, **BrPNI-O** has been synthesized *via* bromination of the **PNI-O** core (yield-95%) (Scheme S2†), which underwent Suzuki coupling with various boronic acid derivatives, including phenyl, bithiophene, and thianthranyl, leading to the successful synthesis of **RPNI-O** derivatives (Scheme S3†). Additionally, thioperylenimide (**RPNI-S**) was prepared using a one-pot synthesis approach (Scheme S4†) involving the reaction between the parent **RPNI-O** and a commercial Lawesson's reagent, resulting in the formation of **RPNI-S** compounds. The detailed synthetic procedure and reaction scheme can be found in the corresponding Scheme 1 and Fig. S1–S4 in the ESI.† The synthesized materials were extensively characterized using multinuclear NMR spectroscopy (^{1}H and ^{13}C) and matrix-assisted laser desorption/ionization (MALDI) techniques. Further details of the comprehensive characterization data can be found in the ESI.†

Photophysical properties

UV-vis absorption and fluorescence spectroscopy were employed to investigate the optical properties of **RPNI-O** and **RPNI-S** (Fig. 1, S1–S3† and Table 1). **RPNI-S** exhibited a pronounced 130 nm red shift in absorption maxima ($\lambda_{abs,max}$) from 506 to 636 nm, accompanied by a corresponding 125 nm red shift in emission maxima ($\lambda_{em,max}$) in solution (Fig. 1a and b). This shift is attributed to the stabilization of the lowest unoccupied molecular orbital (LUMO) and destabilization of the highest occupied molecular orbital (HOMO) in **RPNI-S**, indicating decreased LUMO energies (increased electron

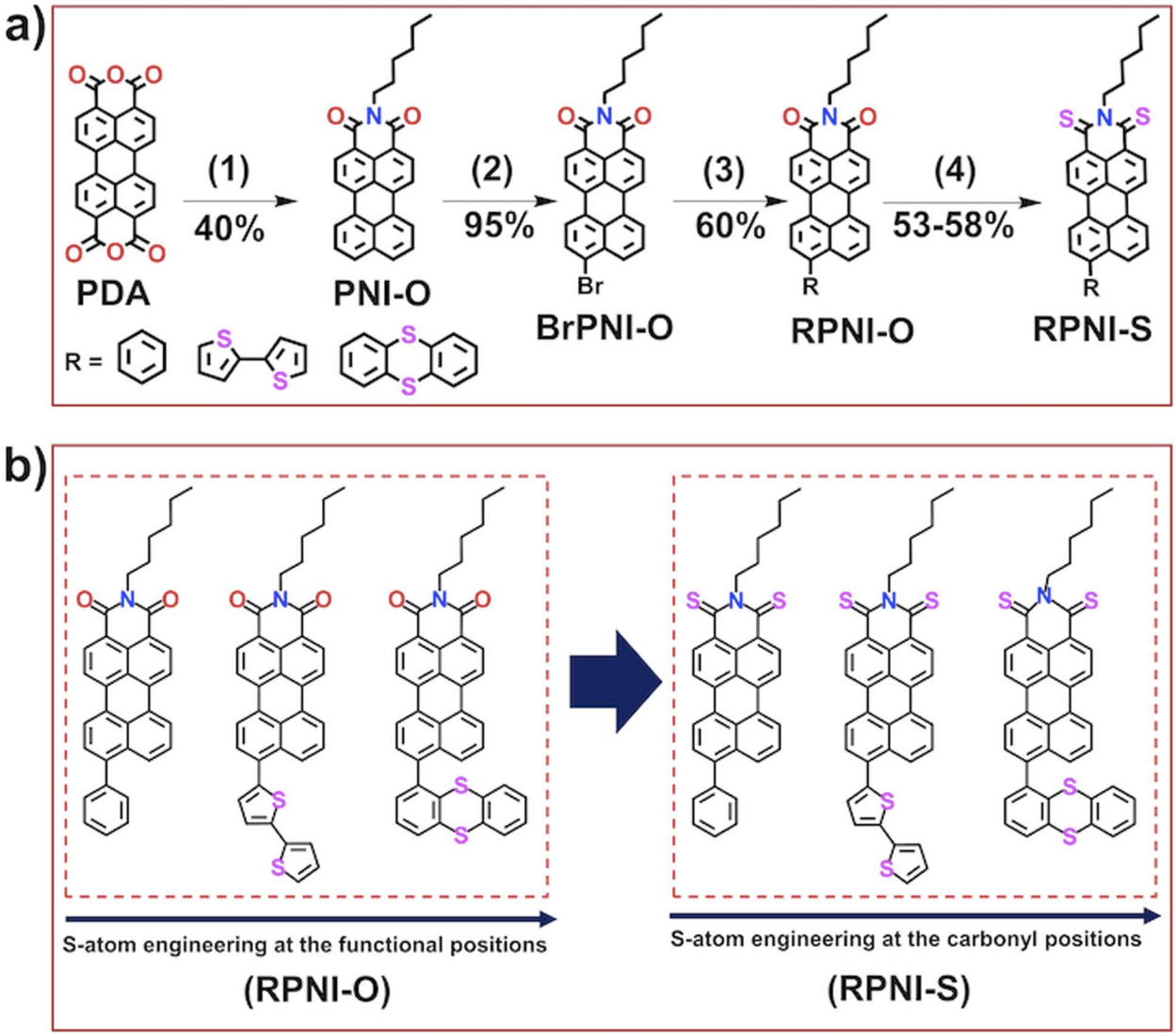

Scheme 1 (a) Synthetic route for the preparation of RPNI-O (PPI, THPI, and API) and thioperylenimides (RPNI-S), *viz.* PPIS, THPIS, and APIS lack an S-atom; instead, the S-atom is positioned within the pendant rotor groups at the *peri*-position of the PNI-O core. (b) Chemical structure of the synthesized RPNI-O and RPNI-S [(1) hexyl amine, H_2O, 20 h, (2) chlorobenzene, Br_2, 4.5 h, (3) Pd(0), THF, H_2O, (4) Lawesson's reagent, toluene, 20 h, and the values below the arrow represents the yield of the corresponding product].

affinity) and increased HOMO energies, resulting in the observed red shift in optical absorption.[14,15,20,21] In contrast, alteration of the S-atom within the pendant functional group (–R) in **RPNI-O** resulted in blue-shifted $\lambda_{abs,max}$ in **API** compared to other **RPNI-O** derivatives, namely **PPI** and **THPI**. This blue shift can be attributed to reduced electronic communication in **API** in its solution state. Crucially, the International Commission on Illumination (CIE) chromaticity diagram vividly displayed a broad spectrum of emission colors in the solution state, ranging from yellow (580 nm) to near-infrared (NIR) at 705 nm (Fig. 1b′, Tables 1 and S3†). **RPNI-O** derivatives, such as **PPI**, showed yellow emission, while **THPI** and **API** displayed bright red emissive colors. In contrast, **RPNI-S** derivatives exhibited emission colors that remained entirely undetectable under 365 nm UV-light illumination, even though $\lambda_{em,max}$ peaks were observed at 655 nm for **PPIS**, 647 nm for **THPIS**, and 705 nm for **APIS**, respectively (Fig. 1b′, Tables 1 and S3†). **API** exhibited notable condensed state emissive properties in its aggregated and solid states, owing to two S-atoms in one fused aromatic anthracene ring (rotor). In contrast, **PPI** and **THPI**, lacking an S-atom at the pendant R rotor and having two S-atoms in two different pendant aromatic rings (rotor), exhibited suppressed emission in their aggregated state. This finding contrasts what is expected based on the RIM mechanism, which typically leads to the generation of condensed state emitters. A detailed explanation of this mechanism is provided through single crystal X-ray diffraction (SCXRD) analysis to shed more light on this discrepancy and provide a comprehensive understanding. Furthermore, **API** exhibits a remarkably high Φ_{PL} of 0.85 in its aggregated state, likely attributed to the unique intermolecular

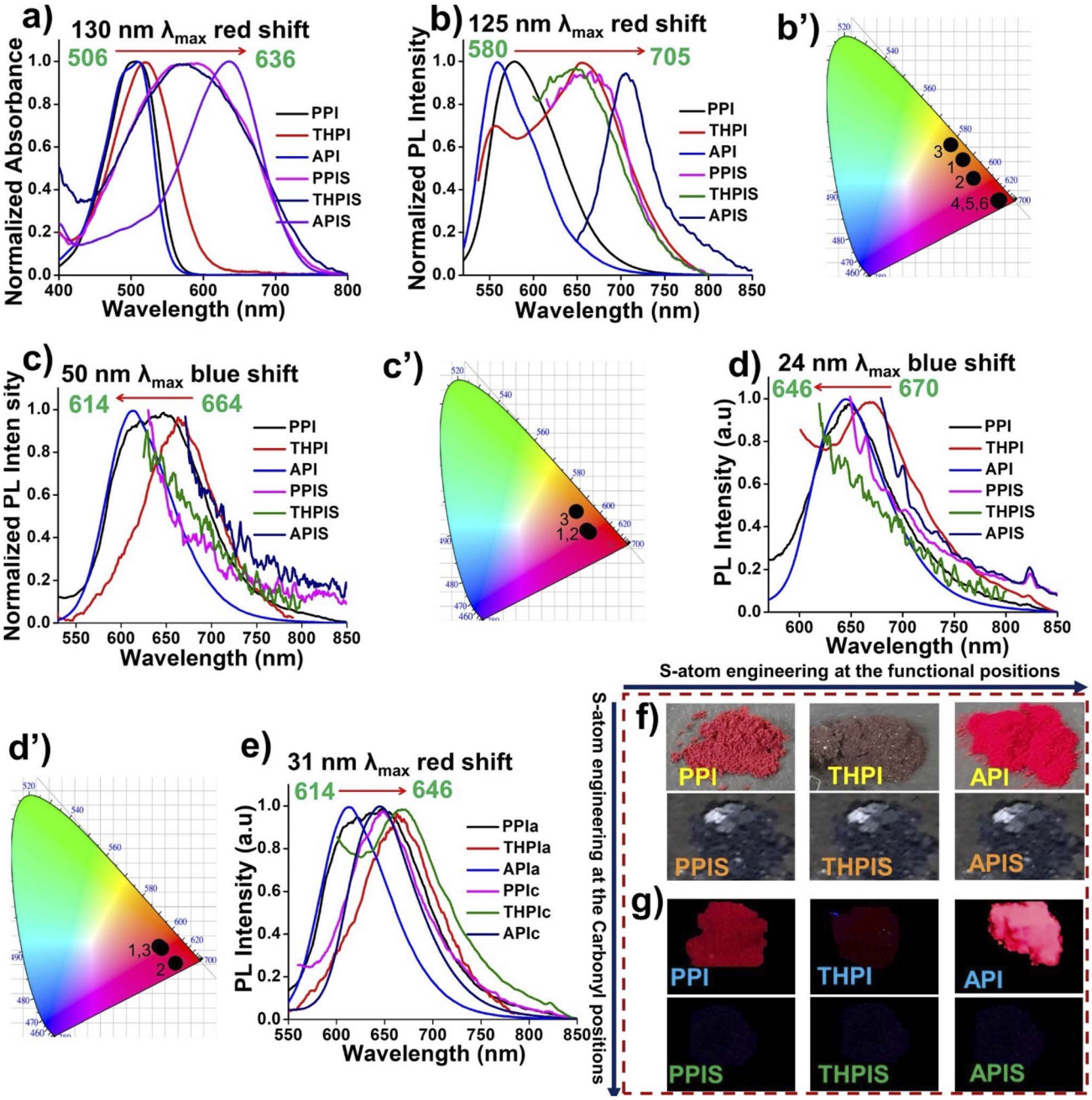

Fig. 1 Photophysical characteristics of all the **RPNI-O** (**PPI**, **THPI**, and **API**) and **RPNI-S** (**PPIS**, **THPIS**, and **APIS**) derivatives. (a) Normalized absorbance spectra in their solution state (in DMSO, 100 μM). (b) The normalized PL spectra in their solution ($\lambda_{ex} = 500$ nm). (b′) The CIE diagram at their solution state. (c) Normalized PL spectra at 99% f_w in DMSO ($\lambda_{ex} = 500$ nm). (c′) The CIE plot represents the aggregated-state emission color. (d) Normalized solid state PL spectra ($\lambda_{ex} = 500$ nm). (d′) CIE plot represents the solid state emission color. (e) Comparison of aggregated-state and solid-state fluorescence spectra of the **RPNI-O** and **RPNI-S** derivatives ($\lambda_{ex} = 500$ nm). Capturing of digital photographs (f) under daylight and (g) under UV irradiation ($\lambda_{ex} = 365$ nm) of solid powder of **RPNI-O** derivatives (**PPI**, **THPI**, and **API**) and **RPNI-S** (**PPIS**, **THPIS**, and **APIS**), respectively. [a and s represent the aggregated and solid state, respectively, inset in CIE: 1, 2, 3, 4, 5, 6 = **PPI**, **THPI**, **API**, **PPIS**, **THPIS**, and **APIS**, respectively. In the (c′ and d′) CIE plot, points 4, 5, and 6 representing the **PPIS**, **THPIS**, and **APIS** were absent due to their non-emissive characteristics].

packing arrangement influenced by self-assembly behavior in its condensed state. Additionally, **API** showed Φ_{PL} of 0.89 in its highest $\lambda_{em,max}$. In contrast, in their aggregated state, other **RPNI-O** derivatives, namely **PPI** and **THPI**, display significantly lower Φ_{PL} of 0.10 and 0.04, respectively. Conversely, the **RPNI-S** compounds exhibited nearly non-fluorescent behavior ($\Phi_{PL} \approx 0.00$) (Table 1, Fig. S2, S3 and eqn (S1)†). The fluorescence suppression indicated that thionation enhanced the ISC process, causing a more efficient transition from the singlet to the triplet excited state.[14,15] The CIE chromaticity diagram

Table 1 Photophysical and photosensitizing characteristics of RPNI-O and RPNI-S derivatives

Materials	[a]λ_{abs} (nm)	[b]λ_{ex} (nm)	[c]λ_{em} (nm)	[d]λ_{em} (nm)	[d]λ_{em} (nm)	[e]Stokes shift (nm)	[f]Φ_{PL}	[g]E_g (eV)	[h]Φ_Δ	[i]ΔE_{ST} (eV)	[j]SOC (cm^{-1})
PPI	506	500	580	646	646	146	0.10	2.60	0.015	1.19	3.81
THPI	510	500	655	664	670	170	0.04	2.51	0.019	0.65	3.50
API	517	500	559	614	646	146	0.85, 0.89	2.70	0.017	1.92	3.13
PPIS	590	550	655	G	G	G	G	2.19	0.04	0.40	10.88
THPIS	590	550	647	G	G	G	G	2.09	0.34	0.42	9.20
APIS	636	630	705	G	G	G	G	2.22	0.26	0.39	5.73

[a] $\lambda_{abs,max}$. [b] λ_{ex}. [c] $\lambda_{em,max}$ represents absorption, excitation, and emission wavelength maxima in the solution state. [d] Aggregated and solid state $\lambda_{em.max}$. [e] Stokes-shift calculated between solid $\lambda_{em.max}$ and $\lambda_{ex.max}$. [f] Φ_{PL} quantum yield in the aggregated state. [g] E_g gaseous-state band-energies. [h] Φ_Δ singlet-oxygen quantum yield. [i] ΔE_{ST} is the first singlet and triplet state energy gap. [j] Spin–orbit coupling between singlet and triplet-states [concentration: 100 μM of **RPNI-O** and **RPNI-S** derivatives in DMSO solution (solution-state), 99% f_w in DMSO (aggregated state), G = not observed].

highlights the distinct emissive colors of **RPNI-O** in their aggregated state. Specifically, **PPI** and **THPI** exhibited quenched emission despite having distinct $\lambda_{em,max}$ peaks, whereas **API** displayed deep red emission. In contrast, **PPIS**, **THPIS**, and **APIS** showed an undetectable $\lambda_{em,max}$ peak and non-emissive features under 365 nm UV irradiation (Fig. 1c′, Tables 1 and S3†). **API** showed a slightly blue-shifted $\lambda_{em,max}$ in the solid state compared to other **RPNI-O** derivatives, with a similar trend observed overall (Fig. 1d and d′). However, when comparing the aggregated states, **API** exhibited a significant 50 nm blue shift in its $\lambda_{em,max}$ compared to **PPI** and **THPI** (Fig. 1c). The validity of this observation was reinforced and elaborated upon using excitation–emission matrix (EEM) spectra. Moreover, **API** displayed a noteworthy 31 nm red shift in its $\lambda_{em,max}$ (646 nm) when in the solid state, compared to the aggregated state (614 nm) (Fig. 1e). This difference can be attributed to the unique intermolecular packing arrangement influenced by the steric constraints of the pendant S-substituted thianthranyl rotor in **RPNI-O**. In contrast, the other derivatives exhibited minimal shifts between their aggregated state and solid state $\lambda_{em,max}$. Further, distinct variations in the powder colors were observed under white light and 365 nm UV irradiation, and this difference correlated well with the CIE chromaticity diagram. **API** showed strong and bright red emission, while **PPI** and **THPI** showed faint emission. **RPNI-S** showed complete emission quenching in its solid state under 365 nm UV light illumination (Fig. 1d′, f, g and Table S3†).

The obtained results provide strong evidence that the presence and positional manipulation of the S-atom within the pendant functional unit played a crucial role in controlling its unique AIE properties.[22–25] Conversely, substituting the S-atom at the carbonyl position leads to distinct characteristics in the condensed state luminescence. Furthermore, all the **RPNI-O** compounds exhibited huge Stokes shifts, ranging from 146 to 170 nm (Table 1). This is noteworthy as it represents the rarest instance of such significant Stokes shifts reported in the literature. These shifts are attributed to an excited-state intramolecular charge transfer (ICT) between the electron donor and acceptor within the dye molecule.[25] The substantial Stokes shifts make these materials highly suitable for bio-imaging applications, as they minimize interference between excitation and emission signals.[26,27]

ACQ-to-AIEE transformation

To explore the influence of aggregation on the fluorescence emission of **RPNI-O** and **RPNI-S** derivatives, UV-vis and photoluminescence (PL) spectra were measured at different water fractions (f_w) in DMSO (Fig. 2, S1, S4, S5, Tables 1 and S4–S6†). **RPNI-O** derivatives (**PPI**, **THPI**, and **API**) displayed distinct absorption peaks at 506 nm, 517 nm, and 490 nm, respectively, characteristic of the π–π* transition associated with the substituted **PNI-O** core. **API** showed an additional long-wavelength absorption peak at 510 nm, attributed to the ICT process from the AIE donor to the acceptor **PNI-O** core. The consistent red-shifted UV and PL spectra in more polar solvents with increasing donor functional groups across **RPNI-O** derivatives suggest a more substantial ICT effect (Fig. S5, Tables S5 and S6†).[28] However, **API** exhibited lesser red-shifted UV and PL spectra than other **RPNI-O** derivatives, indicating reduced D–A interaction and decreased electronic communication in its diluted state. This results in a blue-shifted $\lambda_{abs,max}$ in **API**, distinguishing it from other derivatives. Significant alterations in absorption spectra of **PPI** and **THPI** occurred at 99% f_w, with substantial blue shifts of 60 nm and 46 nm, respectively, indicating H-type aggregation and a strong π–π stacking planar core (Fig. S4a, b and Table S4†). On the other hand, as shown in Fig. S4c and c′† at 0% f_w, **API** displayed characteristic peaks at 490 nm and 510 nm, attributed to the π–π* transition and the ICT peak from the thianthranyl segment to the acceptor **PNI-O** core, respectively.[29–31] As the f_w increased to 99%, the $\lambda_{abs,max}$ at 490 nm gradually red-shifted by 5 nm, accompanied by a red shift of the ICT peak from 510 nm to 536 nm, intensifying more. This red-shifted $\lambda_{abs,max}$ indicates the emergence of J-type aggregation, likely facilitated by the unique intermolecular arrangement of the thianthranyl unit in **API** (Fig. S4c, c′ and Table S4†).[32–36] In contrast to the **RPNI-O** derivatives, the **RPNI-S** derivatives exhibited red-shifted $\lambda_{abs,max}$, with wavelengths of 590 nm, 590 nm, and 636 nm for **PPIS**, **THPIS**, and **APIS**, respectively, at 0% f_w. However, with an increase in water content to 99%, these derivatives displayed remarkable blue shifts in their $\lambda_{abs,max}$, leading to 89 nm, 76 nm, and 23 nm blue shifts, all attributed to the H-type aggregation phenomenon (Fig. S4d–f and Table S4†). This marks the highest reported blue-shifted $\lambda_{abs,max}$ in the aggregated state (Table S2†). The

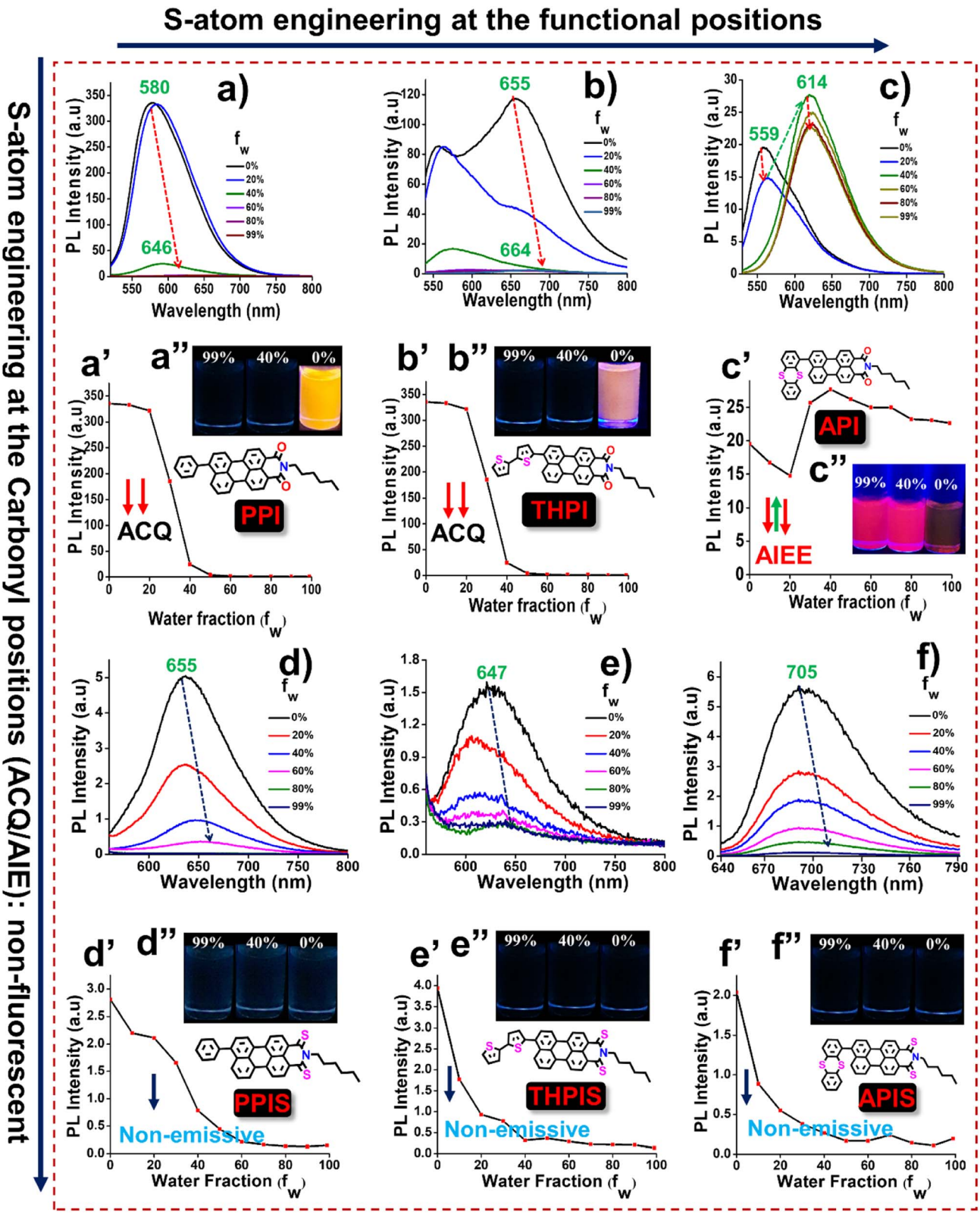

Fig. 2 PL spectra of (a) **PPI**, (b) **THPI**, (c) **API**, (d) **PPIS**, (e) **THPIS**, and (f) **APIS** at various f_w in DMSO (100 μM, $\lambda_{ex} = 500$ nm, for **PPI**, **THPI** and **API**, respectively, $\lambda_{ex} = 550$ nm for **PPIS** and **THPIS**, and $\lambda_{ex} = 630$ nm for **APIS**, respectively). (a′–f′) plots of $\lambda_{em,max}$ along with insets: (a″–f″) digital photographs under 365 nm UV illumination of the corresponding luminogens at 0%, 40%, and 99% f_w in DMSO and chemical structure of the respective **RPNI-O** and **RPNI-S** luminogens, daylight photographs of all the derivatives have been placed in Fig. S6 of the ESI.†

literature has reported the significance of H-aggregation in effectively capturing and stabilizing triplet excited states.[37–39] This highlights the significant impact of the S-atom positional strategy at the functional unit and carbonyl position, as they drastically alter the absorption properties. It is intriguing to note that even though **API** and **APIS** share the same electronic structure, a simple modification involving the introduction of the S-atom at the carbonyl position led to a profound change in their aggregation behavior. In Fig. 2, at 0% f_w, **RPNI-O** (**PPI**, **THPI**, and **API**) showed distinct $\lambda_{em,max}$ peaks at 580 nm, 655 nm, and 559 nm, respectively (Fig. 2a–c, a′–c′, a″–c″ and S1†). With increasing f_w, the emission intensity of **PPI** and **THPI** decreased, becoming completely quenched at 99% f_w, accompanied by a progressive red shift in their $\lambda_{em,max}$ to 646 nm and 664 nm, respectively, known as the ACQ phenomenon. Conversely, **API** exhibited different behavior, with $\lambda_{em,max}$ (located at 559 nm) initially decreasing from 0% to 20% f_w due to twisted intramolecular charge transfer (TICT) characteristics.[28] At 40% f_w, **API** reached maximum emission intensity, with red-shifted $\lambda_{em,max}$ centered at 646 nm, signifying typical AIEE features. However, with more water added, emission intensity decreased due to agglomeration, as illustrated in the supramolecular self-assembly section. The abnormal ACQ behavior of **PPI** and **THPI** in their aggregated state highlights the significant role of the S-atom at the functional unit in **RPNI-O**, energized by intermolecular orientation and packing arrangement.[22,23] In contrast, the **RPNI-S** derivatives exhibited non-emissive characteristics in their solution and aggregated state (Fig. 2d–f, d′–f′, d″–f″ and S1†). When diluted, **RPNI-S** derivatives such as **PPIS**, **THPIS**, and **APIS** exhibited $\lambda_{em,max}$ peaks at 655 nm, 647 nm, and NIR (705) nm, respectively. However, the emission colors were markedly distinct from those of **RPNI-O** derivatives, rendering them undetectable. Furthermore, **RPNI-S** displayed an entirely undetectable $\lambda_{em,max}$ in the aggregated state. This lack of

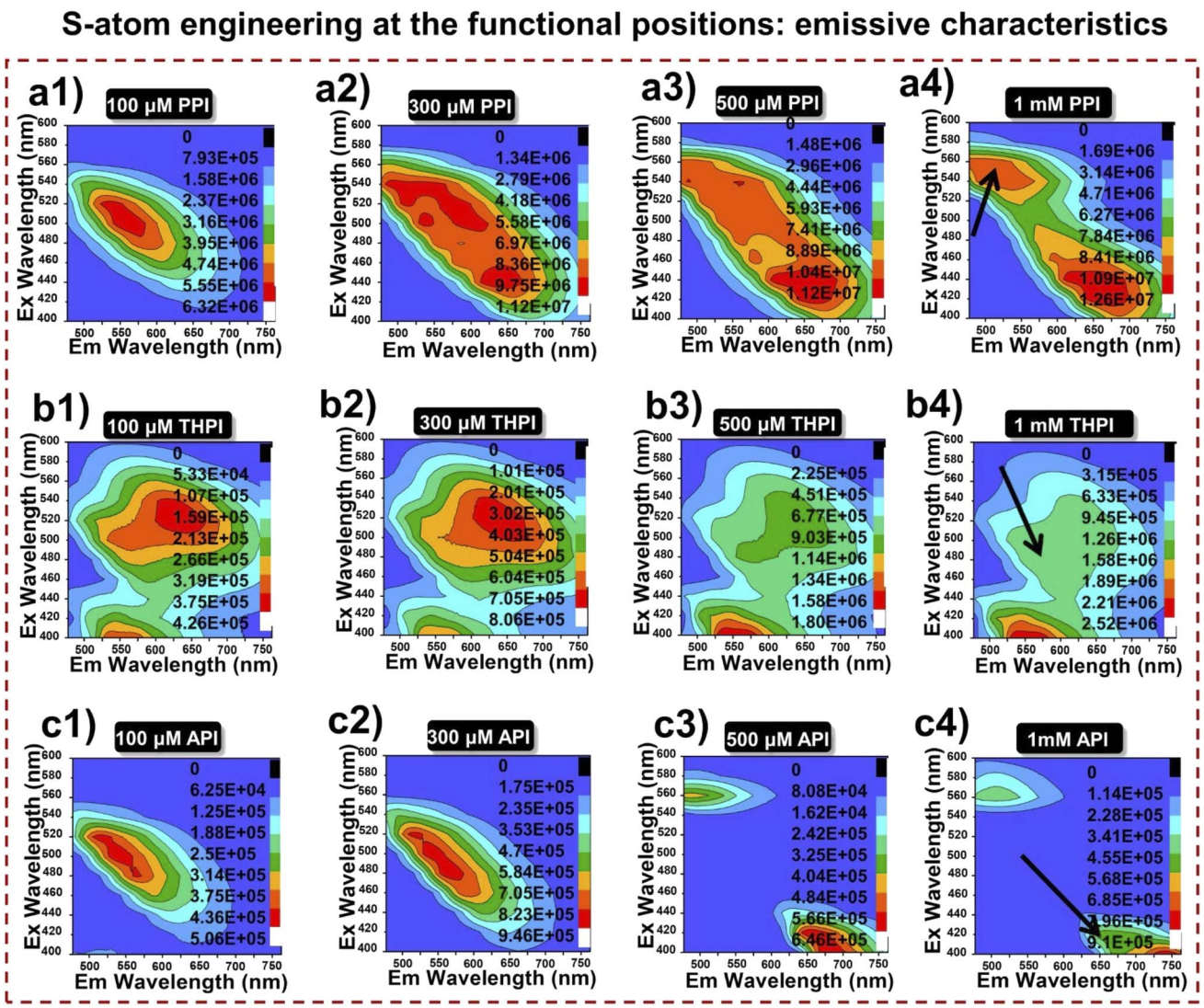

Fig. 3 (a1–c4) 2D EEM contour projections of **RPNI-O** luminogens at different concentrations (left: 100 μM; middle: 300 μM and 500 μM; right: 1 mM) in DMSO [inset: arrow represents the fluorescence intensity].

emission can be attributed to the increased SOC and a higher population of excited state triplets.[14,15]

Excitation–emission matrix spectra

A comparative investigation of the photophysical characteristics of **RPNI-O** and **RPNI-S** derivatives in their condensed state was conducted using EEM spectra (Fig. 3 and S7†). This analysis involved solutions with varying concentrations, providing insights into their optical properties. EEM spectroscopy is recognized for characterizing systems with multiple fluorophores, with each spectrum offering valuable spectral information about chemical components in a mixture.[40] Two-dimensional (2D) EEM spectra were collected for each compound at concentrations of 100 μM (diluted), 300 μM, 500 μM, and 1 mM (concentrated) to examine the effect of concentration on aggregation. For **RPNI-O** derivatives, excitation wavelengths were scanned from 400 to 600 nm in 10 nm increments, with emission values recorded from 500 to 750 nm. Conversely, **RPNI-S** experienced scanning from 500 to 700 nm for excitation, and emission values were measured within 600 to 850 nm. At 100 μM concentration, **RPNI-O** derivatives (**PPI** and **API**) exhibited distinct asymmetric peaks in their EEM spectra, while **THPI** showed partially separated peaks. With increasing concentrations (300 μM and 500 μM), **PPI** and **THPI** displayed broadening in their contour profiles along the *Y*-axis (representing λ_{ex}), indicating the presence of multiple fluorophore components. Conversely, **API** showed two fluorophore systems responding differently to different λ_{ex}, one at higher and the other at lower λ_{ex}. **PPI** and **THPI** exhibited a red-shifted λ_{ex} fluorophore system at higher concentrations, suggesting increased conjugation and enhanced electronic communication between pendant functional units and the **PNI-O** core.[40] In a concentrated solution (1 mM), **PPI** and **THPI** showed weak emission with a red shift in λ_{ex}. At the same time, **API** exhibited a highly emissive system with a blue-shifted λ_{ex} and a non-fluorescent species at higher λ_{ex}. **API** displayed a unique blue-shifted λ_{ex} fluorophore system in its condensed state, attributed to reduced molecular conjugation influenced by the twisted structure of the thianthranyl group within the **PNI-O** core, verified further by SCXRD analysis. **RPNI-S** derivatives displayed weak fluorescence emission at lower concentrations, which diminished completely in a concentrated solution of 1 mM. **THPIS** exhibited a non-emissive fluorophore system with a blue-shifted λ_{ex} compared to **PPIS** and **APIS**. The emission properties were influenced by intermolecular packing interactions and steric constraints imposed by S-atom substitution and

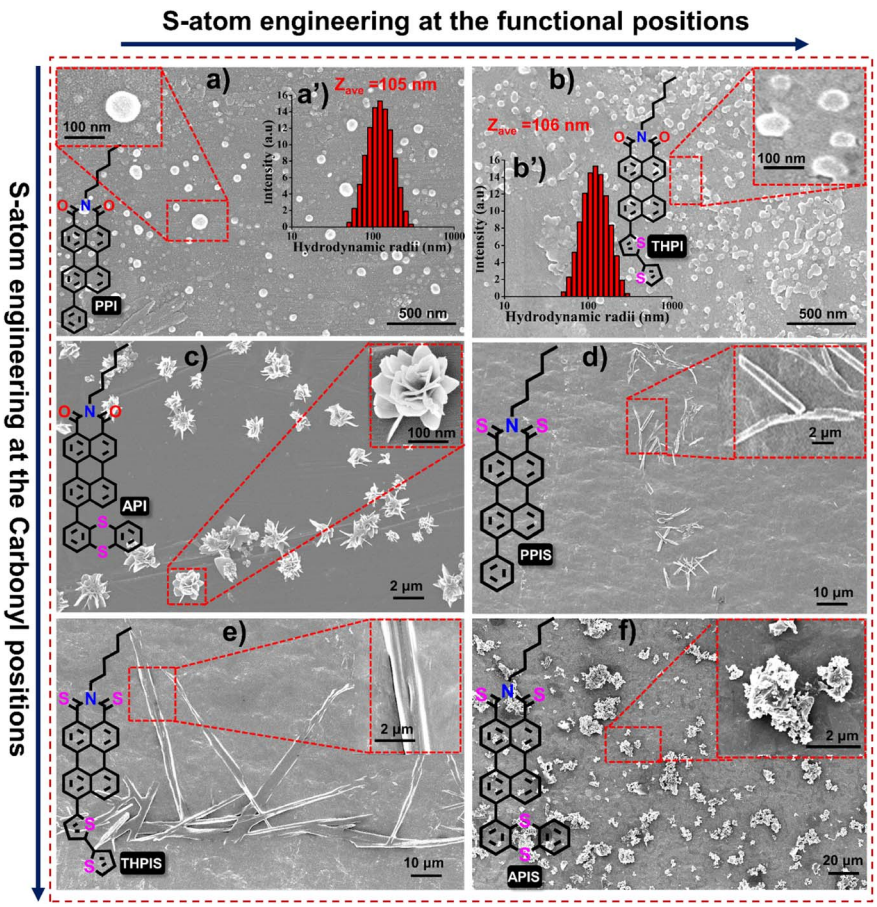

Fig. 4 (a–f) The FESEM images of the micro and nano-assembly of RPNI-O and RPNI-S derivatives spontaneously formed at 99.9% f_w in DMSO (100 μM). Insets: the chemical structure of RPNI-O and RPNI-S (left) and the magnified image at the selected area (right) and left for PPI, and (a′ and b′) hydrodynamic radius *vs.* intensity plot of PPI and THPI at 99.9% f_w in DMSO (100 μM).

positional manipulation at the pendant functional unit in **RPNI-O**. The introduction of the S-atom at the carbonyl position in **RPNI-O** played a critical role in determining non-fluorescent behavior at higher concentrations, differentiating emission characteristics of **RPNI-S** from those of **RPNI-O** derivatives.

Supramolecular self-assembly

The luminescent properties of **RPNI-O** and **RPNI-S** derivatives were investigated using field emission scanning electron microscopy (FESEM) (Fig. 4 and S8†). The FESEM images of the spontaneously formed self-assembled **RPNI-O** and **RPNI-S** derivatives were obtained using a simple, reliable, cost-effective drop-casting method, followed by air-drying at room temperature. Morphological analyses were carried out on the supramolecular assemblies formed at 99% f_w to understand better the fluorescence behavior resulting from aggregation. The remarkable variation in morphological transformation emphasized the exceptional tunability of these **RPNI-O** and **RPNI-S** derivatives, allowing for a wide range of structural possibilities. **RPNI-O** derivatives like **PPI** and **THPI** formed spherical nanoparticles with sizes of 105 nm and 100 nm, respectively, as confirmed by dynamic light scattering (DLS) measurements (Fig. 4a, b, a′ and b′). **API** exhibited unique microrose self-assembly structures, leading to the highest Φ_{PL} generation of 0.85, confirming the discovery of the highest reported Φ_{PL} to date. It is worth noting that the existing literature reports the highest Φ_{PL} value of 0.99 and 0.92, respectively (measurement was conducted in the solution state using an organic solvent such as toluene and dichloromethane as the solvent, respectively), unlike the present work performed in an aqueous environment (aggregated state).[14,15] The unique intermolecular packing arrangement in **API** was determined to be the primary factor contributing to these distinct characteristics (Fig. 4c). **RPNI-S** derivatives, including **PPIS** and **THPIS**, exhibited self-assembly in the form of microcrystalline rods. At the same time, **APIS** displayed a different pattern characterized by micro-agglomeration (Fig. 4d–f). The degree of order in supramolecular self-assembly was directly correlated with the intensity of their emission in the aggregated state.[41–43] In previous literature, it was hypothesized that the decrease in fluorescence emission of AIEgenic materials at higher f_w was due to the formation of agglomerates resulting from stronger stacking interactions.[44] Furthermore, existing literature extensively supports the essential role of energy-dependent endocytosis in the uptake of micro-sized particles. Additionally, numerous studies have

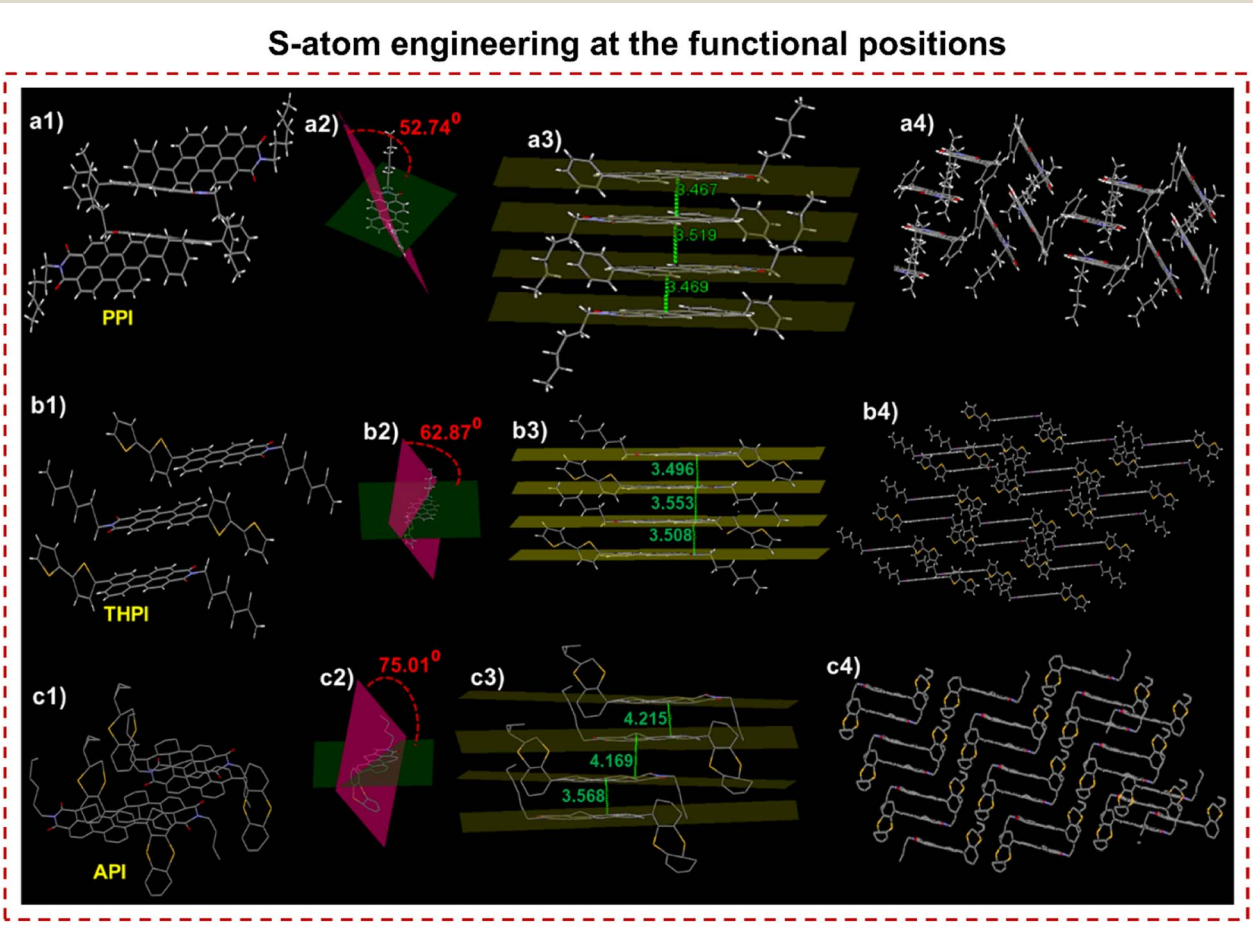

Fig. 5 Single crystal structure of (a1) **PPI**, (b1) **THPI**, and (c1) **API** confirmed *via* SCXRD. (a1–c1) Insight of molecular packing arrangement. (a2–c2) Dihedral angle between two planes of the rotor and acceptor plane. Green plane: perylene core plane, pink plane: the plane of the rotor (phenyl, bithiophene, and thianthranyl in crystals of **PPI**, **THPI**, and **API**). (a3–c3) Intermolecular plane distances and (a4–c4) different molecular packing organization exhibiting J- and H-aggregation patterns, respectively.

highlighted the significant influence of particle morphology on their selective uptake within the intracellular environment.[45,46]

SCXRD analysis

The effects of positional S-substitution within the functional unit were investigated to understand the tuning and triggering characteristics of **RPNI-O** derivatives in the condensed state. This exploration involved a comprehensive analysis of intermolecular interactions and packing arrangements by examining a single crystal (Fig. 5, S9 and Table S7†). **PPI**, **THPI**, and **API** were successfully crystallized from DMF, providing valuable single crystals for analysis. However, attempts to obtain single crystals of other **RPNI-S** derivatives have been unsuccessful. The S-substituted **API**, containing two S atoms within the one fused aromatic ring, exhibits a notably increased intermolecular π–π stacking distance of 4.169 Å compared to other **RPNI-O** derivatives. This phenomenon can be attributed to the highly twisted structure of the pendant thianthranyl unit, as reflected by the larger dihedral angle of 75.01° between the thianthranyl segment and the planar **PNI-O** core. Consequently, this twisted conformation of the thianthranyl segment enlarges the intermolecular distance by increasing the prominent steric hindrance of the planar **PNI-O** core. As a result, the emission quenching in the aggregated state can be prevented due to the remarkably reduced intermolecular π–π stacking interaction.[25,47–50] In contrast, the remaining **RPNI-O** derivatives exhibited robust π–π interactions, likely attributed to their lower dihedral angles between the functional groups and the planar perylene core.[25] Previous research has extensively documented that electron-donating substituents weaken these detrimental π–π interactions by increasing the π-electron density of the aromatic core.[51,52] In contrast, **THPI**, which includes a bithiophene electron-donor functional group with two S-atoms present in two distinct aromatic rings, exhibited a contrary trend. Surprisingly, despite the electron-donating nature of the functional group, **THPI** demonstrated stronger π–π interactions. Moreover, the angle (θ) between the transition dipoles and the interconnected axis was 75.51° for **PPI** and 55.12° for **THPI**. These values exceed the critical threshold of 54.7°, indicating the presence of H-aggregates and further supporting the observed blue-shifted $\lambda_{abs,max}$. Conversely, for **API**, the θ value of 42.08° aligns with the findings of a red-shifted $\lambda_{abs,max}$, further supporting J-type aggregation (Fig. S9†).[38]

This confirms that the strategic manipulation of the S-atom position at the functional unit plays a crucial role in generating distinct intermolecular packing orientations, forming unique and well-defined supramolecular assemblies. Consequently, this manipulation of intermolecular packing orientations leads to the corresponding modulation of their condensed state properties.[53]

Electronic properties driving the photophysical behavior

To validate the hypothesis concerning the distinct electronic properties of **RPNI-O** and **RPNI-S** derivatives and their impact on photophysical behavior, a computational analysis using density functional theory (DFT) using the B3LYP/6-31G(d,p) method was conducted (Fig. 6a) in a gaseous state. This analysis aimed to gain deeper insights into these derivatives' electronic structure and characteristics. The investigation demonstrated that **RPNI-S** derivatives exhibited a significant stabilization of the LUMO and, simultaneously, a destabilization of the HOMO compared to **RPNI-O**. Consequently, the decrease in the energy gap (E_g) between the HOMO and LUMO from 2.70 to 2.09 eV supports the observed more pronounced red-shifted $\lambda_{abs,max}$.[14,15] The presence of its electron-donating bithiophene group primarily contributed to **THPIS** exhibiting the smallest E_g among the derivatives. Conversely, **API** exhibited higher E_g compared to other **RPNI-O** derivatives, attributed to its more stabilized HOMO and less stabilized LUMO. This confirmation accounts for the blue-shifted $\lambda_{abs,max}$ observed in **API** compared to **PPI** and **THPI** in a diluted state. The blue shift indicates reduced electronic communication, resulting from **API**'s more twisted thianthranyl moiety acting as a weaker donor.[25] These results suggest that the S-atom positional engineering prominently influences the electronic properties and modulates its distinct photophysical behavior.

Theoretical calculation

The conversion of **RPNI-O** to **RPNI-S** led to remarkable fluorescence quenching, motivating further theoretical calculations on the optimized structures of **RPNI-O** and **RPNI-S** to understand the triplet state formation mechanism (Fig. 6b, c, Tables 1 and S8–S14†). The spin–orbit coupling matrix elements (SOCMEs) were calculated using ORCA 5.0 at the B3LYP/DEF2-SVP level, ensuring a reasonable TD-DFT error. Replacing oxygen with sulfur significantly increased SOC constants and decreased the singlet–triplet energy gap (ΔE_{ST}) for **RPNI-S**. The SOC from the S_2 state to the T_4 state was identified as the dominant contributor to the formation of the excited triplet population. Notably, SOC increased as the electron-donating ability of the –R groups increased. The ΔE_{ST} between the S_2 and the nearest T_4 states reduced gradually from **APIS** (0.098 eV) to **PPIS** (0.096 eV) and further to **THPIS** (0.094 eV), facilitating the efficient ISC process with SOC values of 10.88 cm^{-1}, 9.20 cm^{-1}, and 5.73 cm^{-1} for **PPIS**, **THPIS**, and **APIS**, respectively. Large SOC values were also observed between the lowest state transition of S_1 to T_1 for **RPNI-S** derivatives, with values of 8.33 cm^{-1} for **PPIS**, 6.90 cm^{-1} for **THPIS**, and 4.44 cm^{-1} for **APIS** with the lowest ΔE_{ST} values of 0.4 eV. Additionally, large SOC values were also found for **PPIS** between the transition of S_7 to T_7 (9.16 cm^{-1}) and **THPIS** of S_7 to T_7 (6.19 cm^{-1}), with ΔE_{ST} values of 0.23 eV and 0.25 eV, respectively (Tables S8 and S9†).[39,54,55] It has been documented that H-aggregates efficiently trap and stabilize the excited state triplet through strong π–π coupling.[37–39] Extensive research has focused on enhancing triplet excitons through photoinduced electron transfer or intramolecular charge transfer.[56,57] Enhancing SOC through prominent H-aggregation represents a unique and innovative approach within this domain. Extensive research has consistently affirmed that H-aggregation significantly extends the excited electron's lifetime by suppressing the fluorescence,

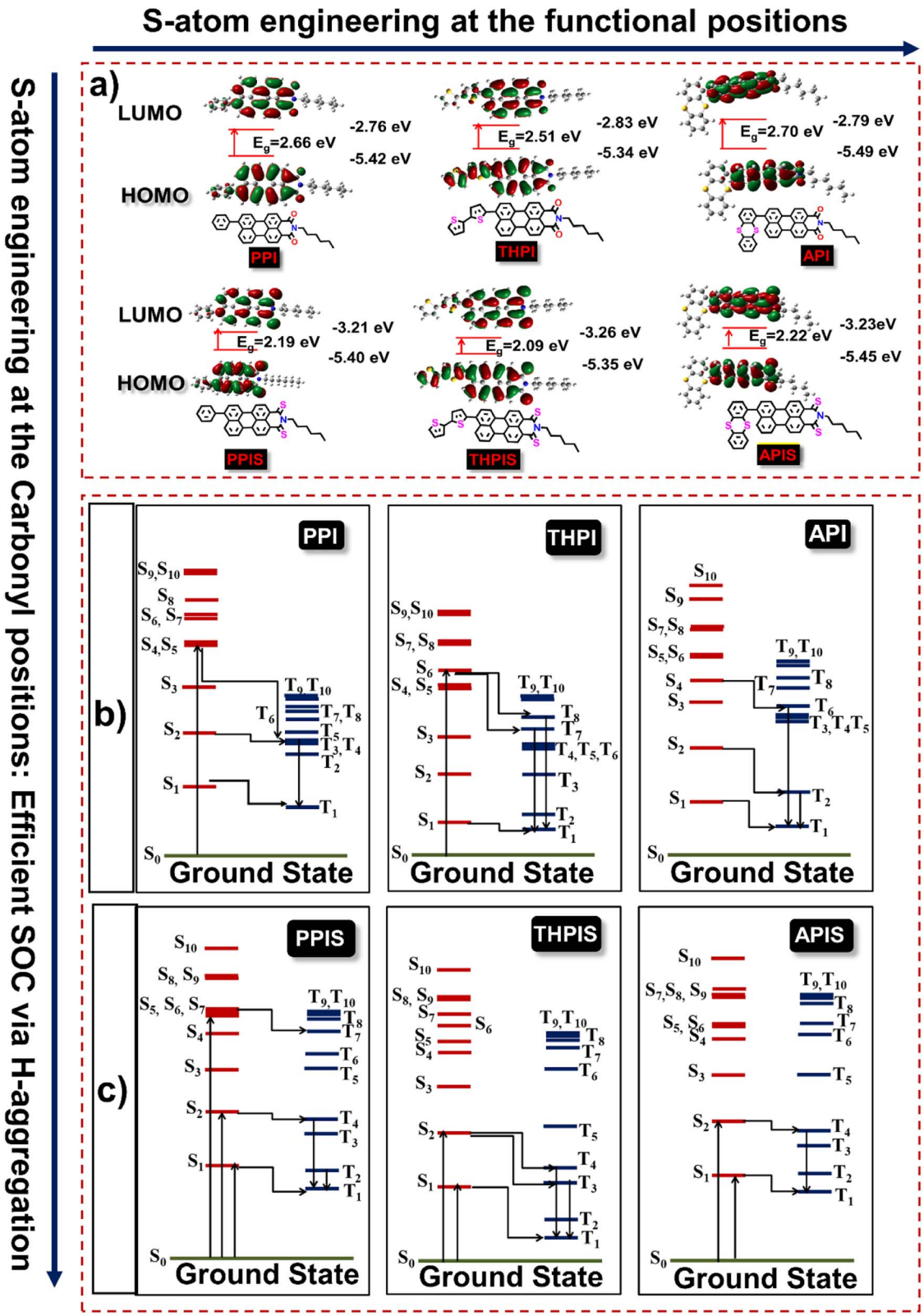

Fig. 6 (a) Frontier molecular orbitals (HOMO and LUMO) with energies in eV calculated from the DFT/B3LYP method using the 6-31G(d,p) basis set by Gaussian 16 software in their ground state. Below is the chemical structure of the respective luminogens. (b and c) SOCME was calculated by the SOC-TDDFT method using ORCA 5.0 software for all the derivatives (**RPNI-O**: **PPI**, **THPI**, and **API**, respectively, and **RPNI-S**: **PPIS**, **THPIS**, and **APIS**, respectively). [**PPI**: $\Delta E_{S_1-T_1} = 1.19$ eV, $\Delta E_{S_2-T_4} = 0.19$ eV, ξ (S_1, T_1) = 0.3 cm^{-1}, and ξ (S_2, T_4) = 3.53 cm^{-1}; **THPI**: $\Delta E_{S_1-T_1} = 0.98$ eV and ξ (S_1, T_1) = 0.65 cm^{-1}; **API**: $\Delta E_{S_1-T_1} = 1.01$ eV, $\Delta E_{S_2-T_2} = 0.23$ eV ξ (S_1, T_1) = 1.92 cm^{-1}, and ξ (S_2, T_2) = 2.36 cm^{-1}; **PPIS**: $\Delta E_{S_1-T_1} = 0.40$ eV, $\Delta E_{S_2-T_4} =$ 0.096 eV, ξ (S_1, T_1) = 8.33 cm^{-1}, and ξ (S_2, T_4) = 10.88 cm^{-1}; **THPIS**: $\Delta E_{S_1-T_1} = 0.42$ eV, $\Delta E_{S_2-T_4} = 0.094$ eV, ξ (S_1, T_1) = 6.90 cm^{-1}, and ξ (S_2, T_4) = 9.20 cm^{-1}; **APIS**: $\Delta E_{S_1-T_1} = 0.39$ eV, $\Delta E_{S_2-T_4} = 0.098$ eV, ξ (S_1, T_1) = 4.44 cm^{-1}, and ξ (S_2, T_4) = 5.73 cm^{-1}].

likely attributed to singlet wavefunction delocalization, which is subsequently energized by the strong π–π coupling. This extension affords sufficient time for the electrons to effectively engage in substantial SOC, which crucially enables the efficient ISC process.[37–39] Interestingly, despite the presence of a less electron-donating phenyl group in **PPIS** compared to the bithiophene in **THPIS**, the SOC value of **PPIS** was found to be greater. The significant blue-shifted $\lambda_{abs,max}$ corroborates the presence of H-aggregation. This difference can be attributed to the more prominent H-aggregation in **PPIS** compared to **THPIS** (Fig. S4, S9, Tables S2 and S4†). Unfortunately, single crystals for the **RPNI-S** derivatives could not be obtained. Nonetheless, a similar type of H-aggregation is anticipated to be observed as with **PPI** and **THPI**, with **RPNI-S** having a larger θ value, making the H-aggregation even more remarkable. **RPNI-S** is derived from **RPNI-O** through a minor modification involving substituting oxygen (O) atoms with S-atoms at the carbonyl position of the **RPNI-O** (Fig. S9†). Notably, Table S2† demonstrates that **RPNI-S** derivatives exhibited significant blue-shifted $\lambda_{abs,max}$ in the aggregated state compared to the previously reported materials.[38,39,55] Herein, the traditional triazine derivative (DPhCzT) and organoboronium $(OB4)_4$ material demonstrate a distinct stabilization of the triplet excited state through H-aggregation, leading to the generation of ultralong phosphorescence.[38,39] This research represents the crucial findings regarding the efficient generation of SOC through pronounced H-aggregation. It is widely explored that SOC plays a pivotal role across various fields, including achieving persistent PL,[58] developing distinct light-emitting materials and devices,[59,60] realizing ultralong room temperature phosphorescence,[61] and development of efficient PSs.[14,15] Extensive research has been devoted to enhancing SOC values in organic compounds, often achieved through strategies such as introducing heavy-atoms[3] or by enhancing the D–A effect.[62–64] In contrast, this study represents a cost-effective and rare design strategy to enhance SOC by incorporating S-atoms at the carbonyl position, avoiding costly heavy-atom incorporation. Importantly, this marks a significant instance of an elevated SOC value compared to previously explored PSs and other conventional organic materials, presented in Table S14a† (it is worth noting that distinct computational methods were employed for each study). In comparison, the reported dibenzofuran compound (**DPBF**) achieved a SOC value of 20.33 cm^{-1}, but it is vital to note that this was based on theoretical studies conducted on aggregated molecules.[61] On the other hand, the heavy-atom-free **NI** and **PDI-4S** PSs exhibited notably high SOC values of 27.8 and 85 cm^{-1}, respectively. Importantly, these values were obtained using a distinct computational methodology, considering significantly more complex molecular systems.[14,15] In contrast, this study unveils a precise and simple design strategy to enhance SOC through S-atom introduction at the carbonyl position, emphasizing the rare mechanism of SOC enhancement *via* promising H-aggregation, which could be energized by the distinct magnitude of the excited triplet state stabilization and prolonging the excited state electron's lifetimes.

Furthermore, the excited state singlet and triplet energies and the corresponding $\Delta E_{S_1-T_1}$ values were lower in **RPNI-S** than **RPNI-O** (Fig. 6b, c, Tables 1, S8–S14 and S14b†). In contrast, **RPNI-O** demonstrated the highest state transition comprising a lower SOC value, which is considered less favorable from a quantum mechanical perspective under identical conditions.

Singlet oxygen (type 2 ROS) detection

Inspired by the remarkable SOC and abundant excited state triplet population in **RPNI-S**, an investigation into their Φ_Δ was conducted using ABDA as a commercially available probe for quantifying $^1O_2$ (Fig. 7a, S10, S11, S12a–c, S13b–d and eqn (S2)†). Table 1 presents the findings, demonstrating that **RPNI-S** displayed moderate Φ_Δ for **PPIS** (0.04), **THPIS** (0.34), and **APIS** (0.26). In contrast, the signal for $^1O_2$ was virtually undetectable for all **RPNI-O** derivatives tested under the same conditions. Notably, the Φ_Δ showed a slight increase with an increase in the electron-donating ability of the –R groups. Thus, the lower Φ_Δ indicates reduced type-II processes for **THPIS** and **APIS** and a complete absence of $^1O_2$ generation for **PPIS**.

Total ROS generation evaluation

In response to the lower Φ_Δ, an evaluation of the overall ROS generation capabilities of **RPNI-S** derivatives was conducted (Fig. 7b, S12d–f, S13a and e–g†). For this purpose, a fluorescent indicator, 2,7-dichlorodihydrofluorescein (DCFDA), known for detecting various types of ROS, was utilized. Under white light irradiation for different durations, DCFDA, in the presence of **RPNI-S** materials, exhibited a gradual increase in PL intensity in their aggregated state (99% PBS fraction in DMSO, f_{PBS}). Interestingly, as the donor functionality increased, the efficiency of ROS generation also increased. After 30 min of light irradiation, DCFDA showed approximately 39-fold, 40-fold, and 29-fold increase in PL intensity in the presence of **PPIS**, **THPIS**, and **APIS**, respectively (Fig. 7b). These results indicate the involvement of both type-I and type-II processes in the ROS generation of **RPNI-S** derivatives. Particularly noteworthy is the remarkable enhancement in PL intensity after just 5 min of white light irradiation, using just 10 μM of DCFDA: **PPIS**, **THPIS**, and **APIS** exhibited enhancements of 2.5×10^5, 1×10^6, and 2×10^5, respectively, while **RPNI-O** derivatives showed lower enhancements of PL intensity (Fig. S13a and e–g†). These findings highlight the rapid and highly efficient production of ROS observed in the **THPIS** PS. This efficiency is attributed to the promising donor bithiophene unit in **THPIS**, setting it apart from other **RPNI-O** and **RPNI-S** derivatives. Consequently, **THPIS** displays the smallest ΔE_{ST} value, facilitating a highly efficient triplet population in the aggregated state.

Type 1 ROS evaluation

To assess the ability of **RPNI-S** to generate free radicals, an electron spin resonance (ESR) experiment was conducted using 2,2,6,6-tetramethyl-4-piperidinol (TEMP) which is widely used as the $^1O_2$ trapper (Fig. 7c and d).[54,65,66] The experiments were performed on **RPNI-S** and **RPNI-O** derivatives in their condensed state (99% f_{PBS}) under white light irradiation. No apparent ESR signal was observed upon white light irradiation, which confirmed the absence of the singlet oxygen generation

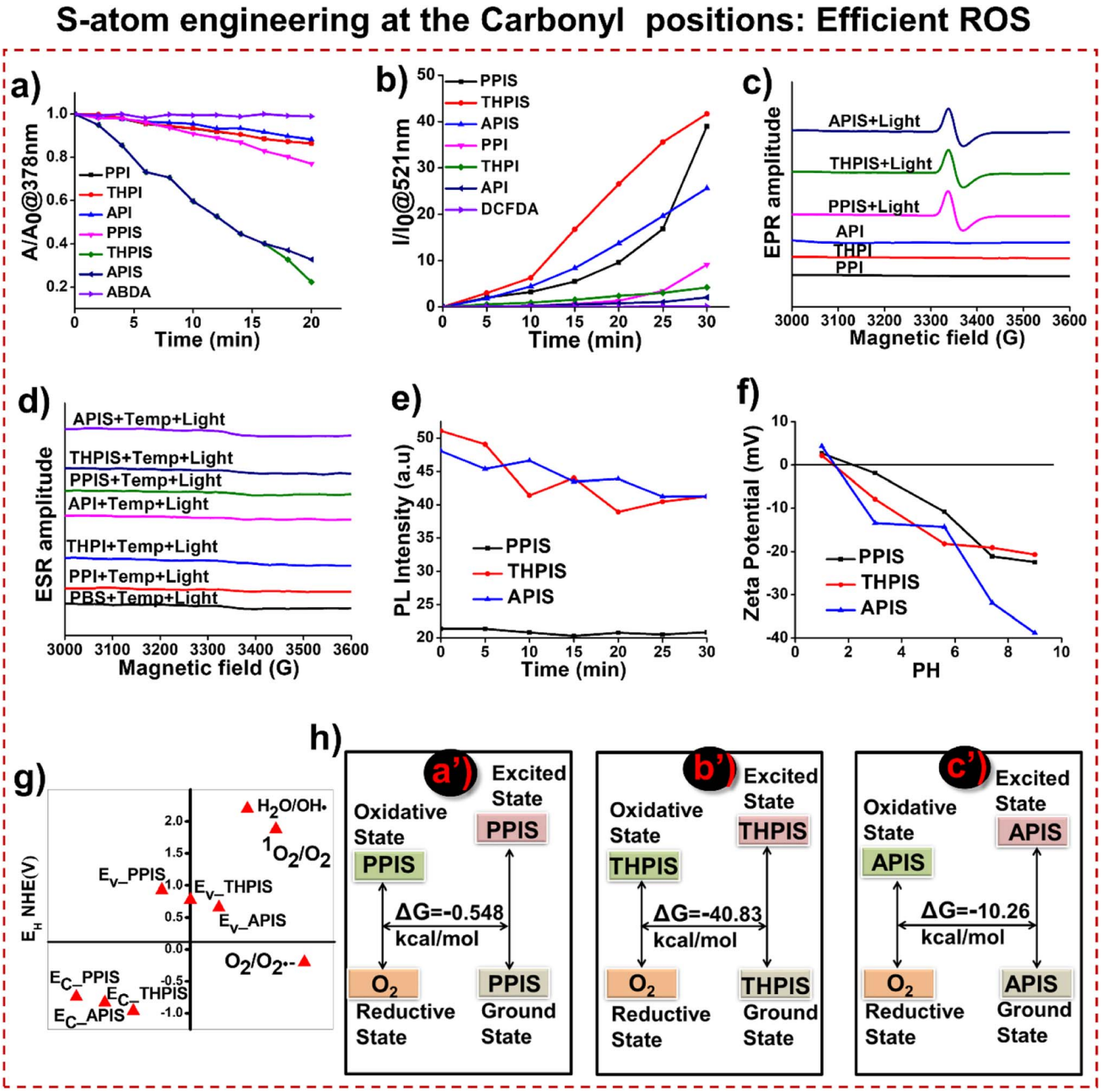

Fig. 7 (a) Plots of ABDA (100 μM) degradation rates at $\lambda_{abs,max}$ of 378 nm by the various PSs (100 μM). (b) Plot of fluorescence intensities of the DCFDA indicator in the presence of **RPNI-O** and **RPNI-S** derivatives. A_0 and A are ABDA absorbance at $\lambda_{abs,max}$ of 378 nm, where I_0 and I are the PL intensities of the indicator at $\lambda_{em,max}$ of 521 nm before and after irradiation of white light, respectively. (c and d) ESR signals of **RPNI-O** and **RPNI-S** derivatives in their solid state without using any trapping agent and TEMP for the $^1O_2$ characterization in the presence of **RPNI-O** and **RPNI-S** derivatives in their aggregated state. (e) PL spectra of TA in the presence of **RPNI-S** derivatives at 528 nm. (f) Zeta potential *versus* pH values of **RPNI-S** derivatives. (g) E_C and E_V of **RPNI-S** derivatives at pH 5.6. The energy scale is expressed concerning NHE. E_H values for $H_2O/HO^•$, $^1O_2/O_2$, and $O_2/O_2^{•-}$ are 2.2, 1.88, and −0.2 eV, respectively. (h) Gibbs free energy changes of (a′) **PPIS**, (b′) **THPIS**, and (c′) **APIS**, respectively, *via* the ORCA 5.0 SOCME module at the B3LYP DEF2-SVP level [aggregated-state: 99% PBS fraction in DMSO, f_{PBS}, and [**RPNI-S**] or [**RPNI-O**] = 100 μM].

ability (Fig. 7d). However, the observation of the ESR signal for **RPNI-S** even without the presence of any trapping agent in the solid state indicates the free radical generation ability and further confirms the effective stabilization of the triplet state (Fig. 7c). This stabilization is attributed to the notable H-aggregation phenomenon exhibited by these derivatives, which leads to the efficient energization of the triplet state, subsequently enhancing its stability.[37–39] In contrast, no ESR signals were observed for **RPNI-O** derivatives under the same conditions. Building upon the type-I process observations, terephthalic acid (TA) was chosen as a fluorescence probe to detect the HO$^•$ radical (Fig. 7e and S14a†).[5,55] The fluorescence intensity of **RPNI-S** probes showed no significant change when TA solutions were subjected to white light irradiation, indicating

that **RPNI-S** did not produce the HO˙ radical. These findings align with the **RPNI-S** derivatives' electrochemical properties and support the type-I PDT mechanism, wherein $O_2^{\bullet-}$ is generated through electron transfer from the triplet excited states to $^3O_2$. Upon evaluating the ROS generation capabilities of these **RPNI-S** derivatives under white light irradiation, the band edge energy levels were estimated using E_{HOMO} and E_{LUMO} (Fig. 7f, g, S14b, c, S15, S16, Tables S15–S17 and eqn (S3)–(S6)†).[55] The points of zero zeta potential for **PPIS**, **THPIS**, and **APIS** were determined to be 2.68, 2.18, and 4.35, respectively (Fig. 7f and Table S15†). The valence band energy (E_V) was determined from X-ray photoelectron spectroscopy (XPS) data (Fig. S15 and Table S17†). The conduction band energy (E_C) was estimated from the E_g obtained from the onset absorption data from UV-visible spectroscopy. It was referenced to the normal hydrogen electrode (NHE) (Fig. S16, Tables S16 and S17†).[55] As a result, the E_C values of **PPIS**, **THPIS**, and **APIS** were found to be −0.74228, −0.83178, and −0.96375 eV at a pH of 5.6, respectively. These values were lower than the redox potential (E_H) of $O_2/O_2^{\bullet-}$ (−0.2 eV) (Fig. 7g and Table S17†). Consequently, all three **RPNI-S** derivatives could transfer electrons to oxygen and generate $O_2^{\bullet-}$, making them suitable PSs for type-I PDT. However, the E_V values of the **RPNI-S** derivatives (0.92772 for **PPIS**, 0.777822 for **THPIS**, and 0.656225 eV for **APIS**, respectively) are smaller than the E_H values of $H_2O/HO^{\bullet}$ (2.20 eV) and $^1O_2/O_2$ (1.88 eV) at a pH of 5.6, suggesting that HO˙ and $^1O_2$ cannot be generated. Consequently, the type-II PDT process is not feasible for **RPNI-S** derivatives (Fig. 7g and Table S17†). On the other hand, **RPNI-O** does produce slight ROS, following the type-I process in PDT, as validated by the experiments involving

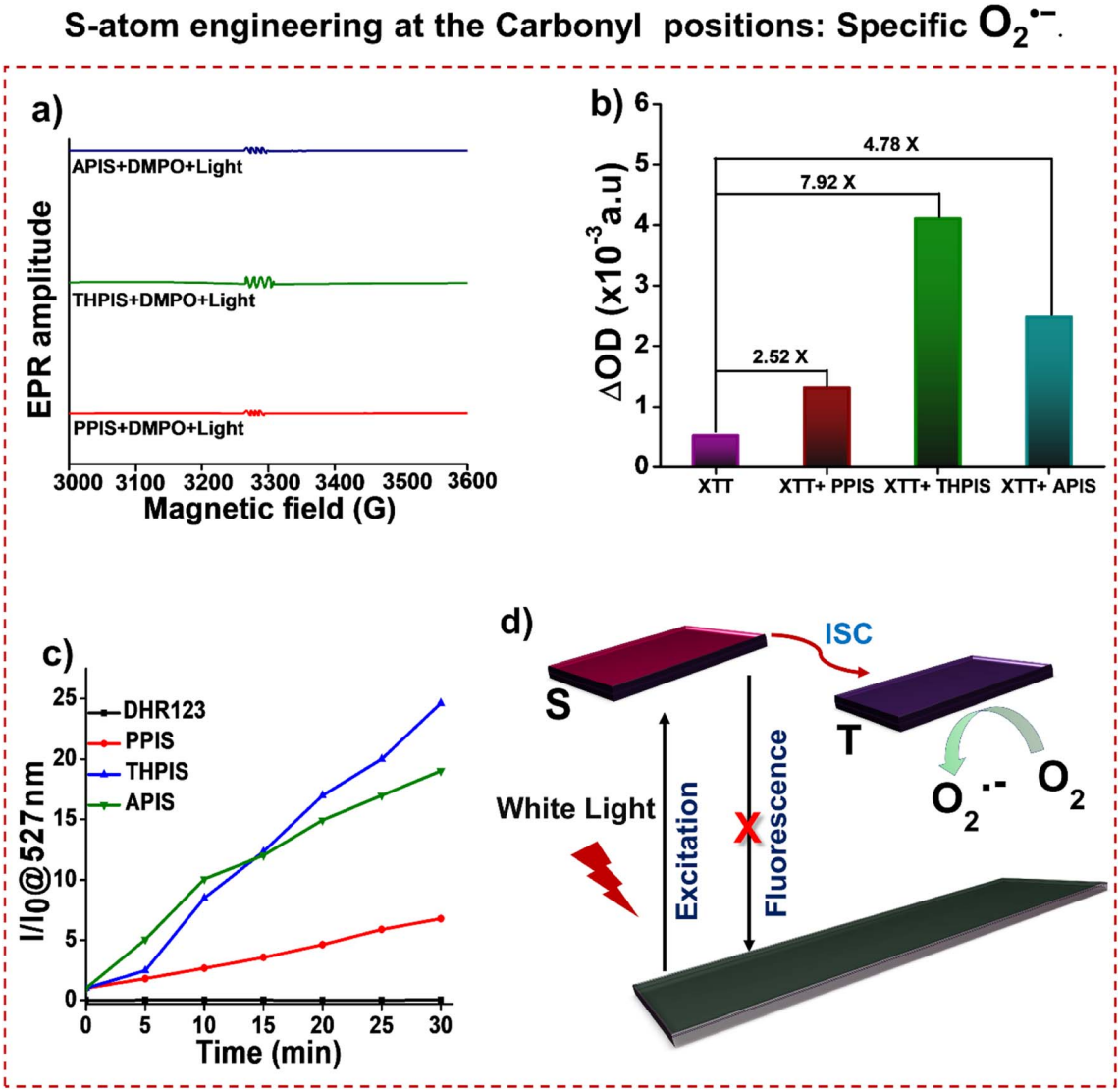

Fig. 8 (a) ESR signals of DMPO for type-I ROS $O_2^{\bullet-}$ characterization in the presence of **PPIS**, **THPIS**, or **APIS** after 10 min white light irradiation in the acetonitrile solution. (b) The UV-vis absorption spectra changes of XTT at 470 nm after being irradiated with white light for 30 min in the presence and absence of **PPIS**, **THPIS**, or **APIS** in the aggregated state. (c) DHR 123 for $O_2^{\bullet-}$ detection in the presence of **PPIS**, **THPIS**, or **APIS** after white light irradiation in the aggregated state. (d) Schematic diagram of white light excitation of **RPNI-S** to produce $O_2^{\bullet-}$ [aggregated state: 99% PBS fraction in DMSO, f_{PBS}, and [**RPNI-S**] = 100 μM].

TA and band energy calculations for NHE (Fig. S14a, c and Table S17†). This result indicates that the driving force for generating $O_2^{\bullet-}$ continuously improves with larger atom sizes of sulfur compared to oxygen.[55]

Furthermore, the feasibility of type-I PDT, specifically in generating $O_2^{\bullet-}$ through the IET mechanism, was investigated by calculating the ΔG values using the ORCA 5.0 quantum mechanics package at the B3LYP/DEF2-SVP level (Fig. 7h and Tables S18–S25†).[54,55] Fig. 7h illustrates that the ΔG value between **THPIS** and O_2 is -40.83 kcal mol^{-1}, which is smaller than the ΔG values of **PPIS** and **APIS** (-0.548 and -10.26 kcal mol^{-1}, respectively). This indicates a higher probability of the IET reaction for **THPIS**. This signifies the exceptionally lower recorded instance of a ΔG value of **THPIS** compared to previously reported PSs. For example, tetraphenylethene (TPE) based PS (TPE-PTB) showed a ΔG value of -14.3839 kcal mol^{-1}. At the same time, the tellurium (Te) comprising PS (PTTe) exhibited a ΔG value of -32.16 kcal-mol^{-1}.[54,55] Based on the theoretical calculations, **THPIS** is theoretically predicted to be the most exceptional type 1 PDT material among the three **RPNI-S** derivatives, efficiently generating $O_2^{\bullet-}$ and slight $^1O_2$. On the other hand, **PPIS** is the second most promising type-I PDT material among the **RPNI-S** derivatives, efficiently generating only $O_2^{\bullet-}$.[5,54,55]

The $O_2^{\bullet-}$ production was further confirmed through electron spin resonance (ESR) spectroscopy, employing 5,5-dimethyl-1-pyrroline-*N*-oxide (DMPO) as the spin-trapping agent. Upon exposure to white light irradiation in the presence of DMPO and **RPNI-S** PSs, the resulting ESR spectrum exhibited an obvious six-line ESR signal (Fig. 8a). These signals originate from the DMPO/$O_2^{\bullet-}$ adduct.[54,67,68] To further validate the $O_2^{\bullet-}$ production ability of the three **RPNI-S**, 2,3-bis(2-methoxy-4-nitro-5-

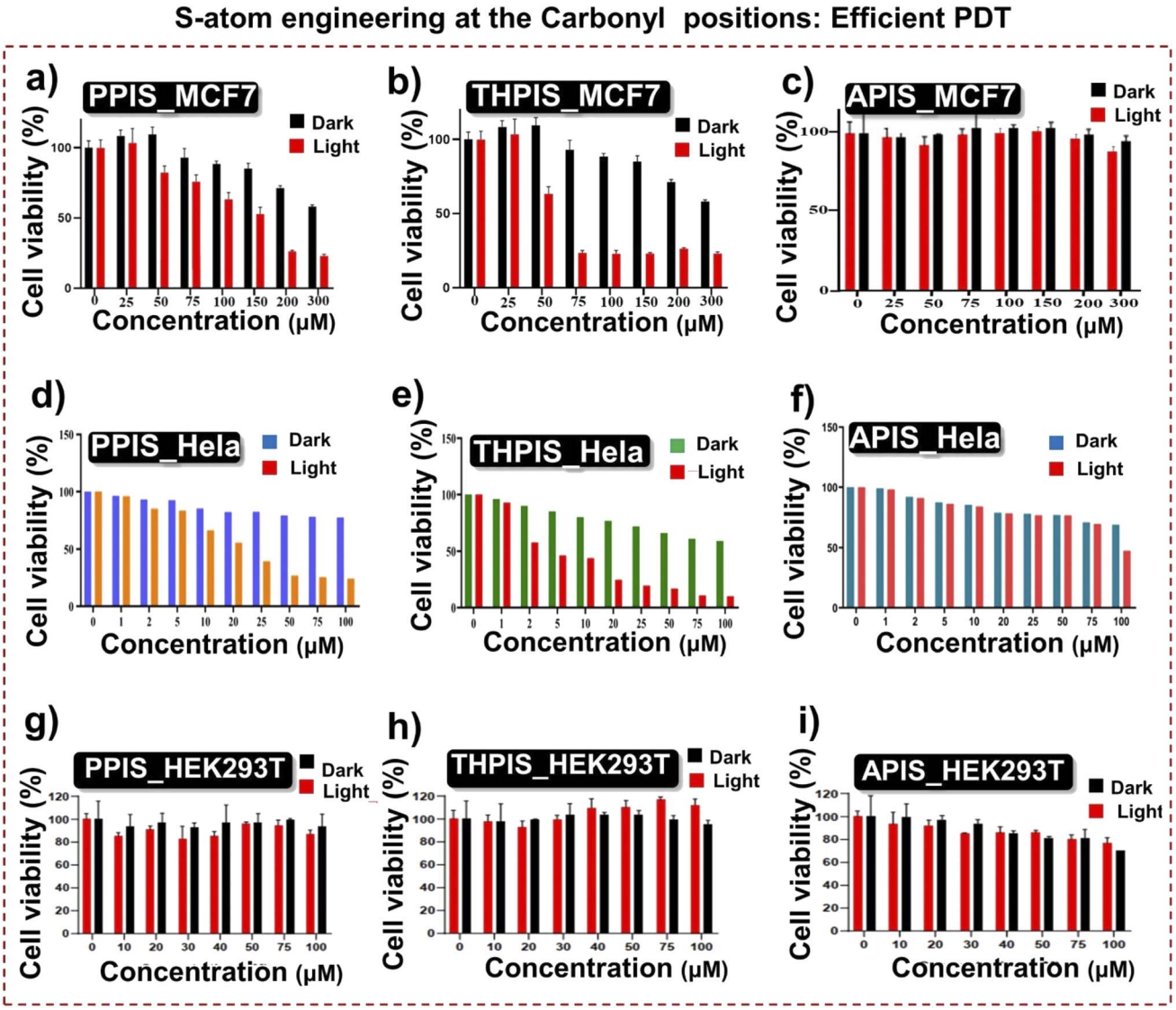

Fig. 9 (a–c) Cell viability of MCF 7 cells after treatment with different concentrations of (a) **PPIS**, (b) **THPIS**, and (c) **APIS**, respectively, along with white light irradiation. (d–f) Cell cytotoxicity of HeLa cells after treatment with different concentrations of (d) **PPIS**, (e) **THPIS**, and (f) **APIS**, respectively, along with white light irradiation. (g–i) Cell viability of HEK293Tcells after treatment with different concentrations of (g) **PPIS**, (h) **THPIS**, and (i) **APIS**, respectively, along with white light irradiation.

sulfophenyl)-2*H*-tetrazolium-5-carboxanilide (XTT) was utilized as an indicator for $O_2^{\bullet-}$ detection. Note that the enhancement in absorption due to XTT formazan occurs upon the interaction of XTT with $O_2^{\bullet-}$. Fig. 8b and S17† showed that continuous enhancement in the absorption intensities of XTT at 470 nm was observed when **PPIS**, **THPIS**, or **APIS** PS were mixed with XTT and exposed to white light irradiation.[69] The changes in probe XTT absorbance were modest but exceeded those documented in the relevant literature.[55,70] Thus, it can be inferred that $O_2^{\bullet-}$ are generated. Notably, the absorption intensity of pure XTT at 470 nm slightly increased. Further $O_2^{\bullet-}$ production was confirmed using dihydrorhodamine 123 (DHR123), which, although non-fluorescent, reacts with $O_2^{\bullet-}$ to emit intense green fluorescence centered at 527 nm.[5,71] As illustrated in Fig. 8c and S18,† the PL intensity of DHR 123 in the presence of **PPIS**, **THPIS**, or **APIS** following 30 min of white light irradiation increased over 5-fold, 25-fold, and 20-fold, respectively, than before irradiation. This suggests a significant $O_2^{\bullet-}$ generation efficiency for **PPIS**, **THPIS**, and **APIS**, respectively (Fig. 8d).

Photodynamic therapy

Efficient ROS generation by **RPNI-S** derivatives prompted *in vitro* PDT studies on HeLa and MCF7 cancer cells, as well as normal cells (Fig. 9). Cellular uptake experiments revealed maximum enrichment of **PPIS**, **THPIS**, and **APIS** in HeLa cells after 4 hours of post-treatment (Fig. S19†).[55] **RPNI-S** derivatives exhibited superior cellular uptake towards HeLa cancer cells at 20 μM concentration while remaining non-toxic to normal cells even at concentrations up to 100 μM. Conversely, **RPNI-O** showed low cellular uptake at 20 μM concentration but was internalized by normal and HeLa cancer cells at 100 μM concentrations (Fig. S20†). Anticancer effects of **RPNI-S** (**PPIS**, **THPIS**, and **APIS**) were investigated in HeLa and MCF7 cancer cells, as well as normal cells, using the MTT assay under dark and light conditions (Fig. 9).[14] **THPIS** and **PPIS** significantly inhibited cell proliferation in HeLa cells with an IC_{50} of approximately 4.5 μM and 15.5 μM, respectively, under 20 minutes of white light irradiation (Fig. 9d–f). A PDT effect was observed in MCF-7 cells at higher concentrations (**PPIS:** ~200 μM and **THPIS:** ~75 μM) (Fig. 9a–c). Notably, **THPIS** and **PPIS** induced approximately 80% cell inhibition at 20 μM and 50 μM concentrations upon light exposure. At 100 μM concentration, **THPIS** exhibited complete cell inhibition, although it showed slight dark toxicity (Fig. 9d–f). **APIS** exhibited negligible cytotoxicity under both dark and light treatments due to its lower cellular uptake, regulated by its anomalous micro-aggregate morphology (Fig. 4f and S19†). **RPNI-S** derivatives showed minimal cytotoxicity towards normal cells in the absence and presence of light, attributed to their optimized cellular uptake mechanism (Fig. 9g–i), which has been strengthened by the precisely controlled morphology in aqueous media (Fig. 4d–f and

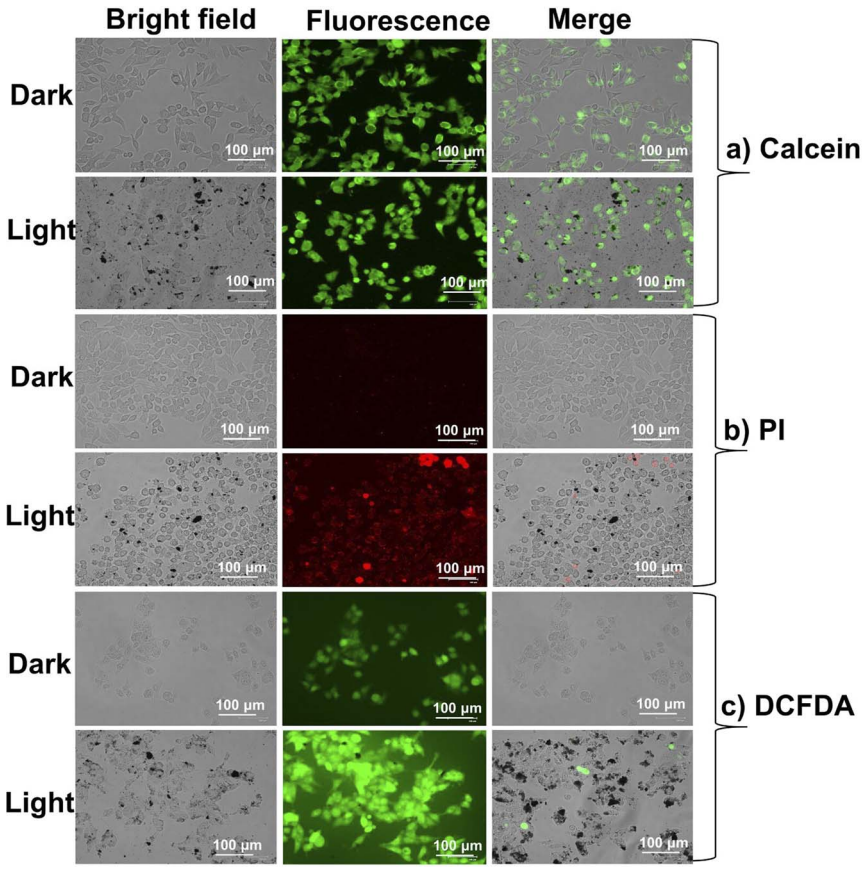

Fig. 10 Fluorescence microscope images of HeLa cells after treatment with PPIS under normoxia and loaded with (a) calcein-AM (2 μM, live cell marker), (b) PI (4 μM, dead cell marker), (c) DCFDA (10 μM, ROS detection probe) [concentration of PPIS: (50 μM), scale bar: 100 μm].

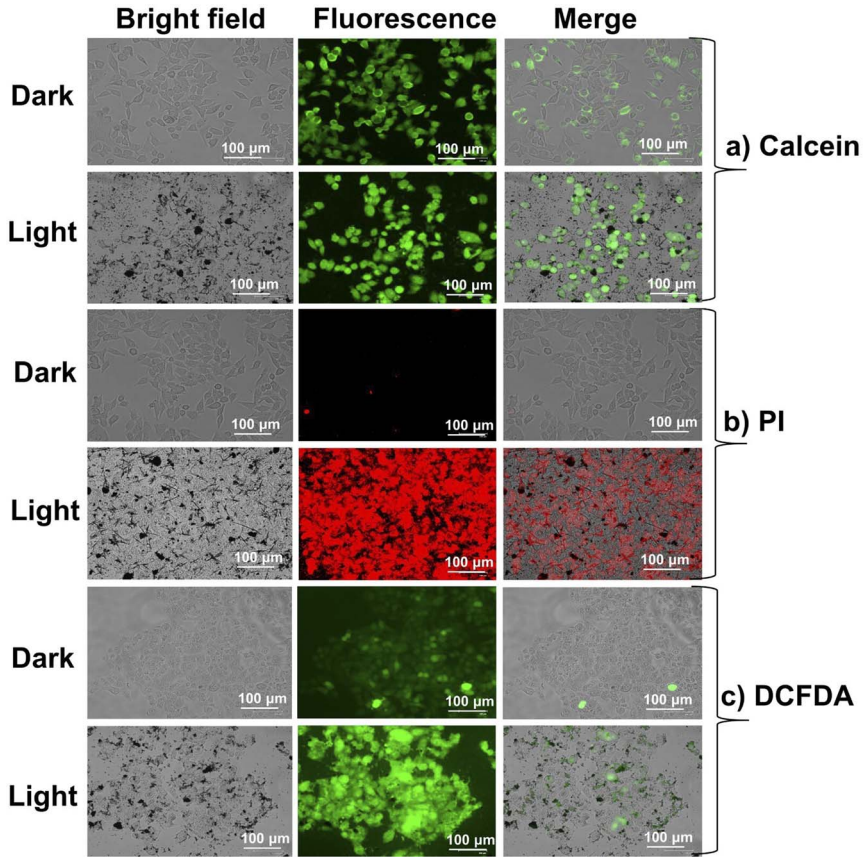

Fig. 11 Fluorescence microscope images of HeLa cells after treatment with THPIS under normoxia and loaded with (a) calcein-AM (2 μM, live cell marker), (b) PI (4 μM, dead cell marker), and (c) DCFDA (10 μM, ROS detection probe) [concentration of THPIS: (50 μM), scale bar: 100 μm].

S19†).[45,46] **RPNI-O** derivatives demonstrated minimal changes upon dark and light treatment towards normal and HeLa cancer cells (Fig. S21†). They predominantly exhibited dark toxicity towards HeLa cells with an IC_{50} of approximately 100 μM, suggesting reduced effectiveness in PDT due to decreased ROS production (Fig. S11, S13† and Table 1). Overall, **RPNI-S** derivatives show promise for broader biological applications due to their superior efficacy and minimal toxicity, supported by optimized cellular uptake mechanisms. Fluorescence microscopy imaging further confirmed the excellent photocytotoxicity of **THPIS** towards HeLa cells (Fig. 10 and 11), highlighting its potential as an exceptional PS. Ongoing research and optimizations hold the potential to enhance its efficacy further and extend its utility in cancer therapy and related fields. However, while **PPIS** has demonstrated the second most promising potential as a PDT material after **THPIS**, ongoing research in our laboratory is currently exploring this approach with **APIS**, utilizing liposomes to enhance its cellular uptake in a biological environment. This enhancement is expected to increase the efficacy of **APIS** PDT in cancer cells correspondingly.

Live cell/dead cell dual staining and intracellular ROS generation

The viability assay, visualized using calcein-AM/propidium iodide, clearly showed the impact of **THPIS**, **PPIS**, and **APIS** on HeLa cells upon white light irradiation (Fig. 10, 11 and S22–S24†).[14] Additionally, intracellular ROS production was confirmed using DCFDA, where green fluorescence was a marker for generating total ROS (Fig. 10c and 11c). These results were consistent with the earlier findings (Fig. 7 and 8). Furthermore, the treated cells exhibited noticeable morphological changes, including reduced size, shrinkage, and cellular collapse under white light irradiation (Fig. 10a–c and 11a–c). These observations further substantiate that **THPIS**-induced photodynamic action enhances outcomes in photodynamic therapy for HeLa cells by inducing organelle destruction. This effect is likely amplified by the efficient accumulation of **THPIS** within HeLa cancer cells, which possess higher cell permeability than normal cells and MCF-7 cancer cells (Fig. S19†). This selective accumulation is facilitated by the precisely controlled morphology of **THPIS** in aqueous media (Fig. 4e and S19†).[45,46] Thus, based on the theoretical and experimental studies regarding ROS generation efficacy, it is plausible to assert that the exceptional PDT efficacy observed in **PPIS** and **THPIS** can be attributed to their pronounced H-aggregation and effective accumulation towards cancer cells. This promising H-aggregation significantly amplifies the SOC and enhances the efficiency of the ISC process during PDT treatment (Fig. 6–8, S4, S19 and Table S2†).[37–39] However, H-aggregation may limit the potential for condensed state applications, and this strategy showed how it could enhance the promising PDT application as well.[22–24,72]

Conclusion

This work suggests that meticulous modulation of the S-atom conformation can lead to enhanced SOC (10.88 cm^{-1}), Φ_{PL} (0.85), and the advancement of potent PSs. Precise incorporation of S-atoms at the pendant functional group in **RPNI-O** showed drastic photophysical properties: Stokes shift of 170 nm, a red-emitting AIEEgen, and established novel AIE mechanisms. Surprisingly, introducing S-atoms at the carbonyl position in **RPNI-O** results in the **RPNI-S** molecule, which exhibits unprecedented structure–property relationships (130 nm red-shifted $\lambda_{abs,max}$, a subsequent extension of $\lambda_{em,max}$ into NIR, and $\Phi_{PL} \approx 0.00$ in the aggregated state). Furthermore, **RPNI-S** established a novel SOC enhancement mechanism *via* prominent H-aggregation. Because the strong π–π coupling is intrinsic in H-aggregation, it efficiently traps and stabilizes the excited state triplet. **RPNI-S** exhibited an efficient IET reaction for type-I PDT, evidenced by an exceptionally lower ΔG value (**THPIS**: −40.83 kcal mol^{-1}). Interestingly, the lower Φ_{Δ}, ΔG, and energy levels suggest the efficient production of $O_2^{\bullet-}$ and minimal type-II ROS ($^1O_2$) for **THPIS**. Herein, **PPIS** is very specific and mainly generates $O_2^{\bullet-}$. The biocompatible and very specific heavy-atom-free **PPIS** and **THPIS** PSs have been shown to have selective and efficient PDT efficacy under normoxia, which is exceptionally rare. Thus, this S-atom positional engineering provides a conceptually important perspective for the potential development of efficient PSs *via* pronounced H-aggregation and distinct condensed state emitters for unique applications.

Data availability

All the data has been included in the ESI file.†

Author contributions

MNK and PKI designed the experiments. MNK synthesized the materials and conducted all the experiments. MNK and PKI wrote and thoroughly revised the manuscript. SN and HR carried out the *in vitro* cellular studies. SN, HR, SK and SSG analysed the data. All authors discussed the results and contributed to the manuscript.

Conflicts of interest

The authors declare no conflicts of interest.

Acknowledgements

The authors extend their gratitude for financial support from the Department of Electronics & Information Technology, specifically DeitY project no. 5(9)/2012-NANO (Vol. II), the Department of Science and Technology (DST) with grant no. DST/SERB/EMR/2014/000034, and the DST-Max Planck Society, Germany, under grant no. IGSTC/MPG/PG(PKI)/2011A/48. Additionally, the authors express appreciation to the Centre for Nano-Technology and the Central Instruments Facility at IIT Guwahati for providing essential instrumental resources. The authors sincerely thank Prof. Aditya Narayan Panda (for his invaluable assistance with the intricate theoretical calculations) and Prof. Mohd Qureshi (for his significant help in conducting preliminary synthetic studies), whose expertise and guidance have been instrumental in shaping the direction and depth of this work.

References

1 B. M. Luby, C. D. Walsh and G. Zheng, *Angew. Chem., Int. Ed.*, 2019, **58**, 2558–2569.
2 A. P. Castano, P. Mroz and M. R. Hamblin, *Nat. Rev. Cancer*, 2006, **6**, 535–545.
3 S. Kolemen, M. Işık, G. M. Kim, D. Kim, H. Geng, M. Buyuktemiz, T. Karatas, X.-F. Zhang, Y. Dede, J. Yoon and E. U. Akkaya, *Angew. Chem., Int. Ed.*, 2015, **54**, 5340–5344.
4 Y. Cakmak, S. Kolemen, S. Duman, Y. Dede, Y. Dolen, B. Kilic, Z. Kostereli, L. T. Yildirim, A. L. Dogan, D. Guc and E. U. Akkaya, *Angew. Chem., Int. Ed.*, 2011, **50**, 11937–11941.
5 M. Li, J. Xia, R. Tian, J. Wang, J. Fan, J. Du, S. Long, X. Song, J. W. Foley and X. Peng, *J. Am. Chem. Soc.*, 2018, **140**, 14851–14859.
6 G. J. Kavarnos and N. J. Turro, *Chem. Rev.*, 1986, **86**, 401–449.
7 L. Shi, F. Hu, Y. Duan, W. Wu, J. Dong, X. Meng, X. Zhu and B. Liu, *ACS Nano*, 2020, **14**, 2183–2190.
8 J. M. Brown and W. R. Wilson, *Nat. Rev. Cancer*, 2004, **4**, 437–447.
9 M. Pollum, S. Jockusch and C. E. Crespo-Hernández, *J. Am. Chem. Soc.*, 2014, **136**, 17930–17933.
10 O. Reelfs, Y.-Z. Xu, A. Massey, P. Karran and A. Storey, *Mol. Cancer Ther.*, 2007, **6**, 2487–2495.
11 L. Martínez-Fernández, I. Corral, G. Granucci and M. Persico, *Chem. Sci.*, 2014, **5**, 1336–1347.
12 K. M. Farrell, M. M. Brister, M. Pittelkow, T. I. Sølling and C. E. Crespo-Hernández, *J. Am. Chem. Soc.*, 2018, **140**, 11214–11218.
13 S. Mai, M. Pollum, L. Martínez-Fernández, N. Dunn, P. Marquetand, I. Corral, C. E. Crespo-Hernández and L. González, *Nat. Commun.*, 2016, **7**, 13077.
14 V.-N. Nguyen, S. Qi, S. Kim, N. Kwon, G. Kim, Y. Yim, S. Park and J. Yoon, *J. Am. Chem. Soc.*, 2019, **141**, 16243–16248.
15 C. Liu, C. Ji, Z. Fan, R. Ma and M. Yin, *Chem. Commun.*, 2021, **57**, 13126–13129.
16 K. Pal, V. Sharma, D. Sahoo, N. Kapuria and A. L. Koner, *Chem. Commun.*, 2018, **54**, 523–526.
17 N. Yang, S. Song, J. Ren, C. Liu, Z. Li, H. Qi and C. Yu, *ACS Appl. Bio Mater.*, 2021, **4**, 5008–5015.
18 C. Li and H. Wonneberger, *Adv. Mater.*, 2012, **24**, 613–636.
19 A. Jana, L. Bai, X. Li, H. Ågren and Y. Zhao, *ACS Appl. Mater. Interfaces*, 2016, **8**, 2336–2347.
20 M. Hussain, J. Zhao, W. Yang, F. Zhong, A. Karatay, H. G. Yaglioglu, E. A. Yildiz and M. Hayvali, *J. Lumin.*, 2017, **192**, 211–217.

21 A. J. Tilley, R. D. Pensack, T. S. Lee, B. Djukic, G. D. Scholes and D. S. Seferos, *J. Phys. Chem. C*, 2014, **118**, 9996–10004.
22 J. Mei, Y. Hong, J. W. Y. Lam, A. Qin, Y. Tang and B. Z. Tang, *Adv. Mater.*, 2014, **26**, 5429–5479.
23 J. Mei, N. L. C. Leung, R. T. K. Kwok, J. W. Y. Lam and B. Z. Tang, *Chem. Rev.*, 2015, **115**, 11718–11940.
24 N. Meher, S. Panda, S. Kumar and P. K. Iyer, *Chem. Sci.*, 2018, **9**, 3978–3985.
25 K. Chen, R. Zhang, Z. Wang, W. Zhang and B. Z. Tang, *Adv. Opt. Mater.*, 2020, **8**, 1901433.
26 J. Luo, Z. Xie, J. W. Y. Lam, L. Cheng, H. Chen, C. Qiu, H. S. Kwok, X. Zhan, Y. Liu, D. Zhu and B. Z. Tang, *Chem. Commun.*, 2001, **18**, 1740–1741.
27 B.-K. An, S.-K. Kwon, S.-D. Jung and S. Y. Park, *J. Am. Chem. Soc.*, 2002, **124**, 14410–14415.
28 S. Sasaki, G. P. C. Drummen and G.-I. Konishi, *J. Mater. Chem. C*, 2016, **4**, 2731–2743.
29 Y. Li, Z. Zhao, J. Zhang, R. T. K. Kwok, S. Xie, R. Tang, Y. Jia, J. Yang, L. Wang, J. W. Y. Lam, W. Zheng, X. Jiang and B. Z. Tang, *Adv. Funct. Mater.*, 2018, **28**, 1804632.
30 S. Thazhathethil, T. Muramatsu, N. Tamaoki, C. Weder and Y. Sagara, *Angew. Chem., Int. Ed.*, 2022, **134**, e202209225.
31 V. Sathish, A. Ramdass, Z.-Z. Lu, M. Velayudham, P. Thanasekaran, K.-L. Lu and S. Rajagopal, *J. Phys. Chem. B*, 2013, **117**, 14358–14366.
32 D. G. Whitten, L. Chen, H. C. Geiger, J. Perlstein and X. Song, *J. Phys. Chem. B*, 1998, **102**, 10098–10111.
33 S. J. Ananthakrishnan, E. Varathan, V. Subramanian, N. Somanathan and A. B. Mandal, *J. Phys. Chem. C*, 2014, **118**, 28084–28094.
34 F. Tang, C. Wang, J. Wang, X. Wang and L. Li, *ACS Appl. Mater. Interfaces*, 2014, **6**, 18337–18343.
35 B.-K. An, D.-S. Lee, J.-S. Lee, Y.-S. Park, H.-S. Song and S. Y. Park, *J. Am. Chem. Soc.*, 2004, **126**, 10232–10233.
36 S. Das, Y. Li, K. Junge and M. Beller, *Chem. Commun.*, 2012, **48**, 10742–10744.
37 J. Yuan, R. Chen, X. Tang, Y. Tao, S. Xu, L. Jin, C. Chen, X. Zhou, C. Zheng and W. Huang, *Chem. Sci.*, 2019, **10**, 5031–5038.
38 Z. An, C. Zheng, Y. Tao, R. Chen, H. Shi, T. Chen, Z. Wang, H. Li, R. Deng, X. Liu and W. Huang, *Nat. Mater.*, 2015, **14**, 685–690.
39 L. Yang, X. Wang, G. Zhang, X. Chen, G. Zhang and J. Jiang, *Nanoscale*, 2016, **8**, 17422–17426.
40 J. Dong, K. M. Solntsev and L. M. Tolbert, *J. Am. Chem. Soc.*, 2009, **131**, 662–670.
41 Y. Deng, M. Wang, Y. Zhuang, S. Liu, W. Huang and Q. Zhao, *Light: Sci. Appl.*, 2021, **10**, 76.
42 P. S. Marqués, M. Krajewska, B. D. Frank, K. Prochaska and L. Zeininger, *Chem.–Eur. J.*, 2023, **29**, e202203790.
43 J. Ye, X. Huang, Y. Gao, X. Wang, T. Zheng, Y. Lin, X. Liu and G. Ning, *CrystEngComm*, 2015, **17**, 9311–9317.
44 M. Soni, S. K. Das, P. K. Sahu, U. P. Kar, A. Rahaman and M. Sarkar, *J. Phys. Chem. C*, 2013, **117**, 14338–14347.
45 J. J. Rennick, A. P. R. Johnston and R. G. Parton, *Nat. Nanotechnol.*, 2021, **16**, 266–276.
46 D. Zhang, L. Wei, M. Zhong, L. Xiao, H.-W. Li and J. Wang, *Chem. Sci.*, 2018, **9**, 5260–5269.
47 Q. Li, Y. Li, T. Min, J. Gong, L. Du, D. L. Phillips, J. Liu, J. W. Y. Lam, H. H. Y. Sung, I. D. Williams, R. T. K. Kwok, C. L. Ho, K. Li, J. Wang and B. Z. Tang, *Angew. Chem., Int. Ed.*, 2020, **59**, 9470–9477.
48 T. Zhang, J. Zhang, F.-B. Wang, H. Cao, D. Zhu, X. Chen, C. Xu, X. Yang, W. Huang, Z. Wang, J. Wang, Z. He, Z. Zheng, J. W. Y. Lam and B. Z. Tang, *Adv. Funct. Mater.*, 2022, **32**, 2110526.
49 D. Wang, M. M. S. Lee, G. Shan, R. T. K. Kwok, J. W. Y. Lam, H. Su, Y. Cai and B. Z. Tang, *Adv. Mater.*, 2018, **30**, 1802105.
50 Y. Li, J. Zhuang, Y. Lu, N. Li, M. Gu, J. Xia, N. Zhao and B. Z. Tang, *ACS Nano*, 2021, **15**, 20453–20465.
51 X. Zhang, L. Du, W. Zhao, Z. Zhao, Y. Xiong, X. He, P. F. Gao, P. Alam, C. Wang, Z. Li, J. Leng, J. Liu, C. Zhou, J. W. Y. Lam, D. L. Phillips, G. Zhang and B. Z. Tang, *Nat. Commun.*, 2019, **10**, 5161.
52 F. Cozzi, M. Cinquini, R. Annuziata and J. S. Siegel, *J. Am. Chem. Soc.*, 1993, **115**, 5330–5331.
53 A. S. Davydov, in *Theory of Molecular Excitons*, ed. A. S. Davydov, Springer US, Boston, MA, 1971, pp. 153–243.
54 Y. Li, R. Tang, X. Liu, J. Gong, Z. Zhao, Z. Sheng, J. Zhang, X. Li, G. Niu, R. T. K. Kwok, W. Zheng, X. Jiang and B. Z. Tang, *ACS Nano*, 2020, **14**, 16840–16853.
55 K. Wen, H. Tan, Q. Peng, H. Chen, H. Ma, L. Wang, A. Peng, Q. Shi, X. Cai and H. Huang, *Adv. Mater.*, 2022, **34**, 2108146.
56 M. A. Filatov, S. Karuthedath, P. M. Polestshuk, H. Savoie, K. J. Flanagan, C. Sy, E. Sitte, M. Telitchko, F. Laquai, R. W. Boyle and M. O. Senge, *J. Am. Chem. Soc.*, 2017, **139**, 6282–6285.
57 Z. E. X. Dance, S. M. Mickley, T. M. Wilson, A. B. Ricks, A. M. Scott, M. A. Ratner and M. R. Wasielewski, *J. Phys. Chem. A*, 2008, **112**, 4194–4201.
58 Y. Dou, C. Demangeat, M. Wang, H. Xu, B. Dryzhakov, E. Kim, T. Le Bahers, K.-S. Lee, A.-J. Attias and B. Hu, *Nat. Commun.*, 2021, **12**, 3485.
59 Z. He, W. Zhao, J. W. Y. Lam, Q. Peng, H. Ma, G. Liang, Z. Shuai and B. Z. Tang, *Nat. Commun.*, 2017, **8**, 416.
60 J. Li, Q. Yao, L. Wu, Z. Hu, B. Gao, X. Wan and Q. Liu, *Nat. Commun.*, 2022, **13**, 919.
61 H. Ma, Q. Peng, Z. An, W. Huang and Z. Shuai, *J. Am. Chem. Soc.*, 2019, **141**, 1010–1015.
62 M. Wang, T. Chatterjee, C. J. Foster, T. Wu, C.-L. Yi, H. Yu, K.-T. Wong and B. Hu, *J. Mater. Chem. C*, 2020, **8**, 3395–3401.
63 Z. Yang, Z. Zhang, Y. Sun, Z. Lei, D. Wang, H. Ma and B. Z. Tang, *Biomaterials*, 2021, **275**, 120934.
64 R. Singh, D.-G. Chen, C.-H. Wang, C.-C. Wu, C.-H. Hsu, C.-H. Wu, T.-Y. Lai, P.-T. Chou and C.-T. Chen, *J. Mater. Chem. B*, 2022, **10**, 6228–6236.
65 Y. Wan, G. Lu, W.-C. Wei, Y.-H. Huang, S. Li, J.-X. Chen, X. Cui, Y.-F. Xiao, X. Li, Y. Liu, X.-M. Meng, P. Wang, H.-Y. Xie, J. Zhang, K.-T. Wong and C.-S. Lee, *ACS Nano*, 2020, **14**, 9917–9928.
66 X. Shi, S. H. P. Sung, J. H. C. Chau, Y. Li, Z. Liu, R. T. K. Kwok, J. Liu, P. Xiao, J. Zhang, B. Liu, J. W. Y. Lam and B. Z. Tang, *Small Methods*, 2020, **4**, 2000046.

67 J. Wang, Y. Hou, W. Lei, Q. Zhou, C. Li, B. Zhang and X. Wang, *ChemPhysChem*, 2012, **13**, 2739–2747.
68 P. Xiao, Z. Shen, D. Wang, Y. Pan, Y. Li, J. Gong, L. Wang, D. Wang and B. Z. Tang, *Adv. Sci.*, 2022, **9**, 2104079.
69 Y. Li, W. Zhang, J. Niu and Y. Chen, *ACS Nano*, 2012, **6**, 5164–5173.
70 L. Brunet, D. Y. Lyon, E. M. Hotze, P. J. J. Alvarez and M. R. Wiesner, *Environ. Sci. Technol.*, 2009, **43**, 4355–4360.
71 J. S. Nam, M.-G. Kang, J. Kang, S.-Y. Park, S. J. C. Lee, H.-T. Kim, J. K. Seo, O.-H. Kwon, M. H. Lim, H.-W. Rhee and T.-H. Kwon, *J. Am. Chem. Soc.*, 2016, **138**, 10968–10977.
72 Z. Yan, H. Xu, S. Guang, X. Zhao, W. Fan and X. Y. Liu, *Adv. Funct. Mater.*, 2012, **22**, 345–352.